Τμήμα Μαθηματικών & Εφαρμοσμένων Μαθηματικών

ΠΑΝΕΠΙΣΤΗΜΙΟ ΚΡΗΤΗΣ

University of Crete
Department of Mathematics and
Applied Mathematics

PhD Thesis in Applied Mathematics

Imaging multiple reflectors in strongly scattering media.

Michael I. Apostolopoulos

supervised by
Prof. Chrysoula Tsogka

Doctoral Committee:

Nikolaos K. Efremidis, Associate Professor
Evangelos A. Harmandaris, Assistant Professor
Dr. Nikolaos A. Kampanis, Research Director
Dimitrios A. Mitsoudis, Assistant Professor
Michael Plexousakis, Assistant Professor
Michael I. Taroudakis, Professor
Chrysoula Tsogka, Professor

June 28, 2016

Acknowledgments

I would first like to give a big Thank You to my supervisor professor Chrysoula Tsogka for being a big encouragement along the way and throughout the course of this work since without her this dissertation would not have been possible. Also I would like to thank all the members of the dissertation committee for the feedback and review that helped to produce this document.

On a personal note, I would like to thank my family including my parents, my wife Iokasti and my little son Yiannis. You always see the potential in others. Thank you for helping me to achieve mine.

Michael Apostolopoulos
June 28, 2016

Contents

List of Figures

List of Tables

Abstract

We consider the problem of imaging small defects embedded in strongly scattering media, often called clutter, using an active array of transducers that can play the dual role of emitters and receivers. Our data is the array response matrix collected by sending short pulses from each source and recording the response at all array elements. Imaging in strong clutter is quite challenging because the array data are dominated by noise due to the multiple scattering of the waves with the medium heterogeneities. To successfully image in this regime using simple coherent imaging functionals we follow the methodology of coherent signal enhancement through data filtering. In particular we consider the approach of [14] and seek to select time-frequency windows that contain the coherent echoes from the reflectors we wish to image using the Local Cosine Transform (LCT). The selection is performed by detecting a pattern disruption in the behavior of the singular values of the local-cosine coefficients transformed matrix. Following [2], we also consider two random matrix theory based selection procedures. The first one is image based and selects time-frequency windows using a criterion that examines the maximum of an appropriately normalized migration image. The second one uses a filter [15] to exclude multiple scattering contributions from the data and then selects the time-frequency windows for which the defect is detectable by looking at the largest singular value of the filtered response matrix. The filter proposed in [15] is a rank one projection (ROP) that is very simple to implement and can be combined with the LCT filter. We study the performance of the different approaches with extensive numerical simulations, carried out in a non-destructive testing setup. Our simulations suggest that the combination of the LCT with the ROP filter gives the best results.

Introduction

Overview

In this thesis, we address the problem of detecting and imaging defects in strongly scattering media, a situation that appears in applications such as non-destructive evaluation of concrete [5]. We illustrate in Figure 1, a typical configuration for active array imaging using a linear array of transducers. Our data is the array response matrix $\mathbf{P}(t) = P(t, \vec{\mathbf{x}}_r, \vec{\mathbf{x}}_s)$, for $r, s = 1, \ldots, N$, measured in the time interval $t \in [0, T]$, using an array of transducers that can act both as sources and receivers. The acoustic signal $P(t, \vec{\mathbf{x}}_r, \vec{\mathbf{x}}_s)$ corresponds to the total pressure field recorded on the r^{th} transducer located at $\vec{\mathbf{x}}_r$ when a pulse *f(t)* is sent from the array element located at $\vec{\mathbf{x}}_s$. In some situations, we might also have data for the incident field, *i.e.*, the pressure field recorded on the array in the absence of the reflector.

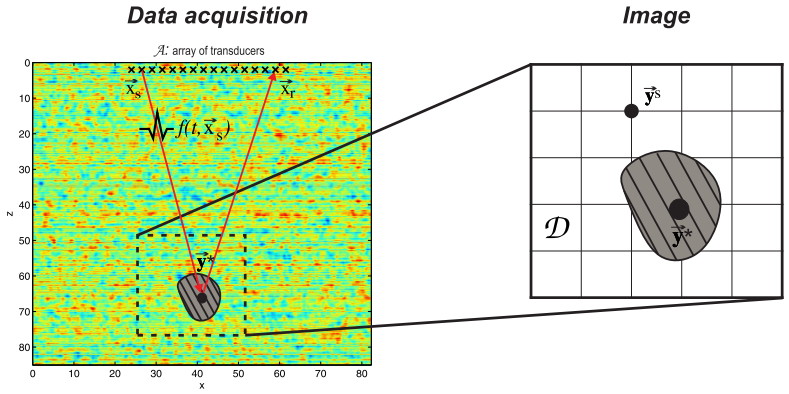

Figure 1: Typical configuration of active array imaging using a linear array of transducers. On the left the data acquisition setup is illustrated. On the right we show an example of an imaging domain. An image is created by associating a value of an imaging functional to each point $\vec{\mathbf{y}}^s$.

The simplest coherent imaging method that one can use to locate reflectors

embedded in homogeneous or weakly heterogeneous media is Kirchhoff Migration (KM). KM has found applications in non-destructive testing [20, 29, 3], optical coherent tomography [28, 27], seismology [11, 31, 10], ultrasonic imaging [26, 33], or in radar [19, 16, 39]. In time domain, KM consists in creating an image by associating the value of the following functional at each point $\vec{\mathbf{y}}^s$ in the search domain,

$$I_{KM}(\vec{\mathbf{y}}^s) = \sum_{r=1}^{N} \sum_{s=1}^{N} P\left(\tau(\vec{\mathbf{x}}_s, \vec{\mathbf{y}}^s) + \tau(\vec{\mathbf{y}}^s, \vec{\mathbf{x}}_r), \vec{\mathbf{x}}_r, \vec{\mathbf{x}}_s\right). \tag{1}$$

This simply consists in evaluating the array data $P\left(t, \vec{\mathbf{x}}_r, \vec{\mathbf{x}}_s\right)$ at time equal to the sum of the travel times from the source to the search point $\tau(\vec{\mathbf{x}}_s, \vec{\mathbf{y}}^s)$ and then from the search point to the receiver $\tau(\vec{\mathbf{y}}^s, \vec{\mathbf{x}}_r)$. The travel times are computed using a model for the background medium. Alternatively, the frequency domain analogue of (1) is

$$I_{KM}(\vec{\mathbf{y}}^s) = \sum_{r=1}^{N} \sum_{s=1}^{N} \int d\omega \hat{P}(\omega, \vec{\mathbf{x}}_r, \vec{\mathbf{x}}_s) exp[-i\omega(\tau(\vec{\mathbf{x}}_s, \vec{\mathbf{y}}^s) + \tau(\vec{\mathbf{y}}^s, \vec{\mathbf{x}}_r))] \tag{2}$$

where $\hat{P}(\omega, \vec{\mathbf{x}}_r, \vec{\mathbf{x}}_s)$ is the Fourier transform of $P\left(t, \vec{\mathbf{x}}_r, \vec{\mathbf{x}}_s\right)$. KM transforms the array data to an image $I_{KM}(\vec{\mathbf{y}}^s)$ by summing over the array elements the back-propagated data from the receiver to the image search point $\vec{\mathbf{y}}^s$ and then back to the source. The point $\vec{\mathbf{y}}^s$ spans the image domain D, as depicted in Figure 1. The back-propagation is performed in (2) using only the phase of the Green's function, however, the amplitude can also be taken into account as is often done in seismic applications [11]. The maxima of the imaging function I_{KM} give estimates as to the location of the reflectors while the image resolution depends on the array size, the distance between the reflectors and the array, the central frequency and the bandwidth of the pulse [11]. KM gives very nice results in smooth media and is very robust to additive noise. In strongly scattering media, however, the coherent echoes from the reflector that we wish to image are overwhelmed by the incoherent field due to the inhomogeneities of the surrounding medium. Consequently, KM produces images that are heavily speckled and peak at unpredictable locations. In order to produce reliable, statistically stable results in clutter, coherent interferometric imaging methods have been established [12, 13, 22]. Nonetheless, this methodology also fails when the target to be imaged is at distance from the array that exceeds one transport mean free path of the scattering medium [36, 13].

We consider here three recently developed filtering methods for successfully imaging in strongly scattering media: (i) the adaptive time-frequency LCT based filter [14], (ii) the rank one projection (ROP) filtering technique [15], which is an alternative to the single scattering filter (SSF) [2], and (iii) a simpler filter that detects the time-frequency windows of interest by defining an image based

criterion such as the maximum of the image normalized by its L_2-norm as presented in [2, 4, 25].

The LCT-based approach proposed in [14] consists in windowing the data in time-frequency windows using the local cosine transform (LCT). Then the window that contains the coherent echoes from the reflectors we wish to image are identified by examining the behavior of the largest singular values of the matrix of the LC coefficients across frequencies. More presicely, in windows that contain clutter echoes only, the singular values are clustered together, whereas, in windows that contain coherent echoes and for a particular frequency range of interest (usually the lower frequencies) the top singular values behave differently. The filter consists in zeroing the LC coefficients in all other windows and in projecting the matrix of LC coefficients on the subspace corresponding to the top singular values in the selected windows and for the selected frequency range. This method is therefore a time-frequency selection procedure that is adaptive and data driven.

The method proposed by Aubry et al. in [2] projects the response matrix on the subspace corresponding to the top singular value, but after applying the single scattering filter (SSF) which is a projection of the data on the subspace that contains single scattering contributions. This approach uses random matrix theory tools to identify the time-frequency windows for which the reflector is detectable. In particular, the probability density function of the largest singular value of the SSF filtered matrix is estimated from the incident field. The ROP filter [15] is an alternative to SSF [2]. The idea is the same, however the projection to the single scattering sub-space is performed in a different way as explained in [15]. From a practical point of view, the procedure followed in SSF is less efficient because half of the array data is disregarded, and that is why we prefer to use the ROP filter. Note that in [15] an additional filter that selects the direction of arrival of the coherent echoes is proposed. Although it significantly improves the results, we do not consider this filter here as we want to focus our attention on the time-frequency selection and compare the results obtained using either the random matrix theory methodology or the LCT-based approach. The direction of arrival selection could be added as the last step on any of the approaches discussed here to further improve the results.

Random matrix theory is used following the approach proposed in [2]. Given data for the incident field, a time-frequency decomposition is performed. The size of the time window is mainly computed so as all the array data from a hypothetical reflector in our search domain can fit in one window in time. The ROP filter is then applied and the largest singular value of the filtered matrix is computed for all windows and frequencies. From these data the power spectral density of the largest singular value is estimated as well as its primitive. Subsequently a probability of false alarm is fixed and this implies a threshold value for the largest singular value.

The procedure of time-frequency decomposition and filtering is repeated on the total field, and time-frequency windows are selected for which the largest singular value is above the threshold set in the previous step. We should note here that, although we mention that the incident field is needed in the random matrix theory approach, it is not needed in the usual sense used in inverse scattering problems but in a rather weaker sense. Instead, what is needed is the incident field for one realization of the cluttered medium, and, in fact not necessarily the same one for which the total field is obtained. This is easier to obtain in practice which makes this approach attractive for non-destructive testing applications.

The dissertation is organized as follows: In Chapter 1 we review some basic facts for the wave equation. In Chapter 2 we formulate the array imaging problem and present the setup for our numerical simulations. All filtering methods used for detection and imaging in strongly back-scattering media are described in Chapter 3. In Chapter 4, we assess the performance of the different filtering techniques with numerical simulations carried out in a non-destructive testing setup. We end with a summary and conclusions.

Chapter 1

The wave equation

1.1 Overview

We present here a few basic facts on the wave equation. We begin with the scalar (acoustic) wave equation in Section 1. We use this equation in the next chapter to write the mathematical model for the data. The pressure field at the sensors is the time convolution of the source excitation and the Green's function described briefly in Section 2. An easy way to deal with convolutions is to work in the Fourier frequency domain, where the wave equation reduces to the Helmholtz equation, as explained in Section 3. We describe there a few important properties of the Green's function and give explicit formulas for the case of homogeneous media.

1.2 The acoustic wave equation

The propagation of sound waves is modeled by a first order system of equations driven by a force $\vec{\mathcal{F}}(t,\vec{\mathbf{x}})$ exerted by an acoustic source. The pressure field $p(t,\vec{\mathbf{x}})$ and the particle velocity $\vec{\mathbf{v}}(t,\vec{\mathbf{x}})$ satisfy the equations of conservation of momentum

$$\varrho(\vec{\mathbf{x}})\frac{\partial\vec{\mathbf{v}}(t,\vec{\mathbf{x}})}{\partial t}+\nabla p(t,\vec{\mathbf{x}})=\vec{\mathcal{F}}(t,\vec{\mathbf{x}}), \tag{1.1}$$

and conservation of mass

$$\frac{\partial p(t,\vec{\mathbf{x}})}{\partial t}+K(\vec{\mathbf{x}})\nabla\cdot\vec{\mathbf{v}}(t,\vec{\mathbf{x}})=0, \tag{1.2}$$

where $t>0$ and $\vec{\mathbf{x}}\in\mathbf{R^n}$. The bulk modulus is indicated by $K(\vec{\mathbf{x}})$ and the mass

density of the medium is given by $\varrho(\vec{\mathbf{x}})$. The source $\vec{\mathcal{F}}(t,\vec{\mathbf{x}})$ is causal supported at $t>0$ and for $t\leqslant 0$ the medium is in its equilibrium state where,

$$p(t,\vec{\mathbf{x}})=0,\vec{\mathbf{v}}(t,\vec{\mathbf{x}})=\mathbf{0}. \tag{1.3}$$

We take the time derivative in (1.2) and substituting (1.1) in order to reduce the first order system (1.1-1.2) to a second order equation for the pressure field. The pressure field $p(t,\vec{\mathbf{x}})$ satisfies

$$\frac{\varrho(\vec{\mathbf{x}})}{K(\vec{\mathbf{x}})}\frac{\partial^2 p(t,\vec{\mathbf{x}})}{\partial^2 t}-\varrho(\vec{\mathbf{x}})\nabla\cdot[\frac{\nabla p(t,\vec{\mathbf{x}})}{\varrho(\vec{\mathbf{x}})}]=-\varrho(\vec{\mathbf{x}})\nabla\cdot[\frac{\vec{\mathcal{F}}(t,\vec{\mathbf{x}})}{\varrho(\vec{\mathbf{x}})}], \tag{1.4}$$

where $t>0$ and $\vec{\mathbf{x}}\in\mathbf{R^n}$. The initial conditions are given by

$$p(0,\vec{\mathbf{x}})=\frac{\partial p(0,\vec{\mathbf{x}})}{\partial t}=0. \tag{1.5}$$

The wave equation takes the canonical form by

$$\frac{1}{c^2(\vec{\mathbf{x}})}\frac{\partial^2 p(t,\vec{\mathbf{x}})}{\partial^2 t}-\Delta p(t,\vec{\mathbf{x}})=F(t,\vec{\mathbf{x}}), \tag{1.6}$$

for $t>0$ and $\vec{\mathbf{x}}\in\mathbf{R^n}$, where the wave speed is

$$c(\vec{\mathbf{x}})=\sqrt{\frac{K(\vec{\mathbf{x}})}{\varrho}}, \tag{1.7}$$

and the source density is

$$F(t,\vec{\mathbf{x}})=-\nabla\cdot\vec{\mathcal{F}}(t,\vec{\mathbf{x}}), \tag{1.8}$$

assuming that ϱ is constant.

1.3 The Green's function - time domain

In order to introduce the mathematical model for the array measurements we need an explicit relation between the pressure field $p(t,\vec{\mathbf{x}})$ and the acoustic source $F(t,\vec{\mathbf{x}})$. Explicitly, we need to invert the wave operator in (1.6), which we denote by $\mathbf{L}$. It is a linear operator defined on the vector space of twice continuously differentiable functions of t and $\vec{\mathbf{x}}$, which vanish together with their time derivative at $t=0$. Equation (1.6) becomes $\mathbf{L}p=F$ and has the unique solution

$$p = \mathbf{L}^{-1} F. \tag{1.9}$$

The inverse $\mathbf{L}^{-1}$ is an integral operator with kernel given by the causal Green's function $G(t, \vec{\mathbf{x}}, \vec{\mathbf{y}})$ and (1.9) is given by the explicit form

$$p(t, \vec{\mathbf{x}}) \;=\; \int_0^t ds \int_{\mathbf{R^n}} d\vec{\mathbf{y}} F(s, \vec{\mathbf{y}}) G(t-s, \vec{\mathbf{y}}, \vec{\mathbf{x}}), \tag{1.10}$$

which is the Duhamel's principle. The causal Green's function satisfies

$$\begin{aligned} \frac{1}{c^2(\vec{\mathbf{x}})} \frac{\partial^2 G(t, \vec{\mathbf{x}}, \vec{\mathbf{y}})}{\partial t^2} - \Delta_{\vec{\mathbf{x}}} G(t, \vec{\mathbf{x}}, \vec{\mathbf{y}}) &= \delta(\vec{\mathbf{x}} - \vec{\mathbf{y}})\delta(t), \qquad \vec{\mathbf{x}}, \vec{\mathbf{y}} \in \mathbf{R^n}, \qquad t > 0, \\ G(t, \vec{\mathbf{x}}, \vec{\mathbf{y}}) &= 0, \qquad t < 0, \end{aligned} \tag{1.11}$$

in the sense of distributions, where $\Delta_{\vec{\mathbf{x}}}$ is the Laplace operator in the $\vec{\mathbf{x}}$ variable, and δ is the Dirac distribution. Note that since both the source and Green's function are causal (supported at positive time), we have

$$\int_0^t ds F(s, \vec{\mathbf{y}}) G(t-s, \vec{\mathbf{x}}, \vec{\mathbf{y}}) = F(t, \vec{\mathbf{y}}) \star_t G(t, \vec{\mathbf{x}}, \vec{\mathbf{y}}), \tag{1.12}$$

and then eq. (1.10) is rewritten as a time convolution

$$p(t, \vec{\mathbf{x}}) = \int_{\mathbf{R^n}} d\vec{\mathbf{y}} F(t, \vec{\mathbf{y}}) \star_t G(t, \vec{\mathbf{y}}, \vec{\mathbf{x}}). \tag{1.13}$$

1.4 The Green's function - frequency domain

We define the Fourier transform as

$$\hat{p}(\omega, \vec{\mathbf{x}}) = \int_{-\infty}^{\infty} dt p(t, \vec{\mathbf{x}}) e^{i\omega t} \tag{1.14}$$

and the corresponding inverse Fourier transform is

$$p(t, \vec{\mathbf{x}}) = \int_{-\infty}^{\infty} \frac{d\omega}{2\pi} \hat{p}(\omega, \vec{\mathbf{x}}) e^{-i\omega t}. \tag{1.15}$$

In the transformations (1.14-1.15) above, ω indicates the angular frequency - measured in radians per second - and the relation between the angular frequency and the frequency ν (measured in Hz) is given by

$$\omega = 2\pi\nu. \tag{1.16}$$

Moreover, the relation between the frequency ω, the wavenumber k and the wavelength λ is described by

$$k = \frac{\omega}{c_0} = \frac{2\pi}{\lambda}, \qquad \lambda = \frac{c_0}{\nu}, \tag{1.17}$$

where c_0 denotes the reference wave speed. In the Fourier (frequency) domain convolutions become products, so then the wave field of (1.13) becomes

$$\hat{p}(\omega, \vec{\mathbf{x}}) = \int_{\mathbf{R^n}} d\vec{\mathbf{y}} \hat{F}(\omega, \vec{\mathbf{y}}) \hat{G}(\omega, \vec{\mathbf{y}}, \vec{\mathbf{x}}), \tag{1.18}$$

where $\hat{G}(\omega, \vec{\mathbf{y}}, \vec{\mathbf{x}})$ is the Fourier transform of the causal Green's function. This is the same as the outgoing Green's function of the Helmholtz equation given by

$$[\Delta_{\vec{\mathbf{x}}} + \frac{\omega^2}{c^2(\vec{\mathbf{x}})}]\hat{G}(\omega, \vec{\mathbf{y}}, \vec{\mathbf{x}}) = -\delta(\vec{\mathbf{x}} - \vec{\mathbf{y}}). \tag{1.19}$$

Note that if we started directly with (1.19), we would have to use the Sommerfeld radiation condition to specify the outgoing Green's function. The Sommerfeld radiation condition is

$$\lim_{|\vec{\mathbf{x}}-\vec{\mathbf{y}}|\to\infty} |\vec{\mathbf{x}} - \vec{\mathbf{y}}|^{(n-1)/2} [\frac{(\vec{\mathbf{x}} - \vec{\mathbf{y}})}{|\vec{\mathbf{x}} - \vec{\mathbf{y}}|} - i\frac{\omega}{c_0}]\hat{G}(\omega, \vec{\mathbf{x}}, \vec{\mathbf{y}}) = 0. \tag{1.20}$$

Two important properties of the Green's function are: the *reciprocity* and the *Kirchhoff-Helmholtz asymptotic identity*. The latter identity, is used for example in resolution analysis and studies of imaging with ambient noise sources [21]. The reciprocity identity,

$$\hat{G}(\omega, \vec{\mathbf{x}}, \vec{\mathbf{y}}) = \hat{G}(\omega, \vec{\mathbf{y}}, \vec{\mathbf{x}}), \tag{1.21}$$

suggests that the wave field at $\vec{\mathbf{x}}$ due to a point source at $\vec{\mathbf{y}}$ is the same as the wave field at $\vec{\mathbf{y}}$, due to a point source at $\vec{\mathbf{x}}$. This statement permits us to switch the role of sources and receivers in the analysis of imaging functions.

The Green's function in 2D and 3D

In three dimensions the Green's function $\hat{G}_0(\omega, \vec{\mathbf{x}}, \vec{\mathbf{y}})$ in homogeneous media is expressed by

$$\hat{G}_0(\omega, \vec{\mathbf{x}}, \vec{\mathbf{y}}) = \frac{e^{ik|\vec{\mathbf{x}}-\vec{\mathbf{y}}|}}{4\pi|\vec{\mathbf{x}}-\vec{\mathbf{y}}|}. \tag{1.22}$$

The two-dimensional Green's function is given by

$$\hat{G}_0(\omega, \vec{\mathbf{x}}, \vec{\mathbf{y}}) = \frac{i}{4} H_0^{(1)}(k|\vec{\mathbf{y}}-\vec{\mathbf{x}}|), \tag{1.23}$$

where the $H_0^{(1)}$ is the zero order Hankel function of the first kind. If we take into account the asymptotic approximation of the $H_0^{(1)}$ at large arguments the expression of (1.23) becomes

$$\hat{G}_0(\omega, \vec{\mathbf{x}}, \vec{\mathbf{y}}) \approx \frac{1}{2}\sqrt{\frac{i}{2\pi k|\vec{\mathbf{x}}-\vec{\mathbf{y}}|}} e^{ik|\vec{\mathbf{x}}-\vec{\mathbf{y}}|} \tag{1.24}$$

It should be noted that in both two and three dimensions the Green's function $\hat{G}_0$ is the product of a smooth amplitude multiplied by the oscillatory

$$\exp(ik|\vec{\mathbf{x}}-\vec{\mathbf{y}}|) = \exp(i\omega\tau(\vec{\mathbf{x}}, \vec{\mathbf{y}})) \tag{1.25}$$

The amplitude of $\hat{G}_0$ is independent of the frequency in three dimensions, but not in two dimensions.

Chapter 2

Imaging problem and numerical setup

2.1 Overview

In this chapter we describe the problem of active array imaging and we present the setup used in our numerical simulations.

2.2 Formulation of imaging problem

We consider the problem of array imaging in strongly back-scattering media, in which the reflections from the object to be imaged are corrupted by the noisy back-scattered field due to the medium heterogeneities. Our data is the array response matrix $\mathbf{P}$(t) obtained by sending pulses *f(t)* from each array transducer $\vec{\mathbf{x}}_s$ and recording the echoes at all receiver elements $\vec{\mathbf{x}}_r$. Wave propagation is governed by the acoustic wave equation,

$$\begin{aligned} \frac{1}{v^2(\vec{\mathbf{x}})}\frac{\partial^2 p(t,\vec{\mathbf{x}})}{\partial t^2} - \Delta p(t,\vec{\mathbf{x}}) &= f(t)\delta(\vec{\mathbf{x}}-\vec{\mathbf{x}}_s), \quad \forall\ \vec{\mathbf{x}}\in\Omega, \quad t>0, \\ p(0,\vec{\mathbf{x}})=0, \quad \frac{\partial p(0,\vec{\mathbf{x}})}{\partial t} &= 0, \quad \forall\ \vec{\mathbf{x}}\in\Omega \end{aligned} \tag{2.1}$$

in an open and unbounded domain $\Omega \subset \mathbf{R^2}$. We assume a broadband pulse

$$f(t) = e^{-i\omega_0 t} f_{B_0}(t)$$

with Fourier transform

$$\hat{f}(\omega) = \int_{-\infty}^{\infty} e^{i(\omega-\omega_0)t} f_{B_0}(t)dt = \hat{f}_{B_0}(\omega - \omega_0), \tag{2.2}$$

supported in the frequency interval centered at ω_0 with bandwidth B_0. The wave speed $v(\vec{\mathbf{x}})$ is described by

$$\frac{1}{v^2(\vec{\mathbf{x}})} = \frac{1}{c^2(\vec{\mathbf{x}})}\left(1 + \varepsilon\mu\left(\frac{x}{\ell}, \frac{z}{\ell_z}\right) + \nu(\vec{\mathbf{x}})\right) \tag{2.3}$$

where $\vec{\mathbf{x}} = (x, z)$. In (2.3), $c(\vec{\mathbf{x}})$ is the smooth part of the velocity. For simplicity we assume, in what follows, that $c(\vec{\mathbf{x}}) = c_0$. The z-axis indicates the direction of propagation, also called range, and the x-axis is the cross-range direction. In (2.3), $\mu\left(\frac{x}{\ell}, \frac{z}{\ell_z}\right)$, is a random function that we use to model the medium inhomogeneities. The length scales ℓ and ℓ_z denote the correlation lengths in the cross-range and range directions, while the parameter ε is the strength of the fluctuations. The term $\nu(\vec{\mathbf{x}})$ is the reflectivity of the object that we wish to image. We assume that $\nu(\vec{\mathbf{x}})$ has compact support and our objective in the imaging problem is to find the support of $\nu(\vec{\mathbf{x}})$ from the given data matrix $\mathbf{P}(t)$. Alternatively, a reflector can be also modeled as an impenetrable scattering body. This is what we will do in our numerical simulations where the reflector is modeled as a soft scatterer by imposing to the pressure field to be zero on its boundary.

2.3 Setup of numerical simulations

We will consider either one or two reflectors embedded in three different types of clutter: isotropic, layered and combined (see Figure 2.1). In all cases, the smooth part of the velocity is constant $c(\vec{\mathbf{x}}) = c_0 = 1$km/s, and the fluctuations are generated with random Fourier series. We select, appropriately, the numerical parameters so as to be in a regime that is typically encountered in ultrasonic non-destructive testing experiments [3]. In the isotropic medium we have, $\mu_i(\vec{\mathbf{x}}) = \mu(\frac{x}{\ell}, \frac{z}{\ell})$, with correlation function

$$E\{\mu_i(\vec{\mathbf{x}}_1)\mu_i(\vec{\mathbf{x}}_2)\} = \left(1 + \frac{|\vec{\mathbf{x}}_1 - \vec{\mathbf{x}}_2|}{\ell}\right) e^{-\frac{|\vec{\mathbf{x}}_1 - \vec{\mathbf{x}}_2|}{\ell}},\ \ell = \lambda_0/4,$$

and standard deviation $\varepsilon_i = 0.1$. In the layered medium, $\mu_l(\vec{\mathbf{x}}) = \mu(\frac{z}{\ell_z})$ with correlation function

$$E\{\mu_l(z_1)\mu_l(z_2)\} = \left(1 + \frac{|z_1 - z_2|}{\ell_z}\right) e^{-\frac{|z_1 - z_2|}{\ell_z}},\ \ell_z = \lambda_0/50,$$

and $\varepsilon_l = 0.17$. In the combined medium, the fluctuations are given by the combination

$$\mu_c(\vec{\mathbf{x}}) = \frac{1}{\sqrt{2}}(\mu_i(\vec{\mathbf{x}}) + \mu_l(\vec{\mathbf{x}}))$$

with $\varepsilon_c = 0.1$. We considered here this combination to give the same weight in the isotropic and layered fluctuations while keeping the std of μ_c equal to one. Any other combination of isotropic and anisotropic fluctuations can be also considered.

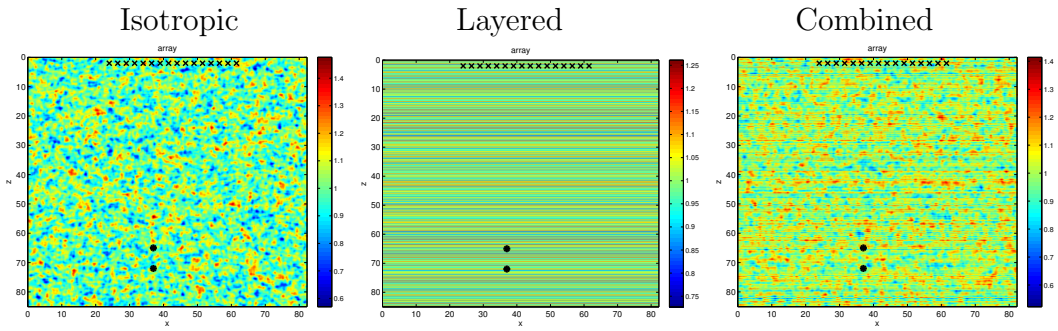

Figure 2.1: The two reflectors embedded in three different cluttered media. Isotropic on the left, layered in the center and combined on the right.

Our array is composed by $N = 80$ elements located at $(x_r, z) = (24\lambda_0 + (r - 1)\frac{\lambda_0}{2}, 2\lambda_0)$, $r = 1, \ldots, N$. To obtain the array response matrix we solve numerically the wave equation in the heterogeneous medium with velocity $v(\vec{\mathbf{x}})$. The pulse $f(t)$ is a Ricker wavelet, a first derivative of a Gaussian, with central frequency $f_0 = 10$MHz and supported in a large bandwidth $[0, 30]$MHz.

Each reflector is a small disk of diameter λ_0 and is modelled as a soft scatterer, *i.e.*, the acoustic field is zero at its boundary. The reflectors that we wish to image are located at $\vec{\mathbf{y}}_1^\star = (37\lambda_0, 65\lambda_0)$, $\vec{\mathbf{y}}_2^\star = (37\lambda_0, 72\lambda_0)$, for all cluttered media, as shown in Figure 2.1 above. From the detection and imaging point of view, this configuration is quite challenging due to the fact that the second reflector $\vec{\mathbf{y}}_2^\star$ is relatively hidden behind the first one $\vec{\mathbf{y}}_1^\star$ with respect to the array elements. In this thesis, we will show results either for two reflectors, or for only one, in which case we consider the first reflector $\vec{\mathbf{y}}_1^\star$ located closer to the array of transducers. Length is measured in units of the central wavelength $\lambda_0 = 0.1$mm.

The numerical method that we use is based on a first order in time formulation of the wave equation with unknowns the velocity (the time derivative of the displacement) and the pressure field. A leap-frog finite difference scheme is used for the discretization in time and mixed-finite elements for the discretization in space. Specifically, the velocity is discretized with piecewise linear basis functions and the pressure field by piecewise constants. The convergence analysis of the

finite element method is carried out in [6, 7]. To model wave propagation in unbounded domains we follow the perfectly matched absorbing layer technique [9]. The methodology is presented in the case of elastic wave propagation in [8] and its generalization to visco-acoustic wave propagation is considered in [24].

Chapter 3

Time-frequency window selection methods

3.1 Overview

In this chapter, we present three newly established filtering methodologies that select time-frequency windows which contain the coherent echoes from the reflectors we wish to image. The first one is a quite simple idea that relies on the values of the imaging functional obtained by backpropagating the windowed data. More precisely a time-frequency window is retained when the maximum value of the image obtained, normalized by its L_2-norm, is above a certain threshold. The important quantity is the value of the threshold which can be determined by studying the statistical distribution of the image values in background media with the same scattering properties in the absence of the reflectors. This method was first proposed in [2] and is also considered in [4, 25]. We describe it briefly in Section 3.2. The second method instead of looking at the corresponding images, selects the appropriate time-frequency windows focusing only on the data, exploiting their singular value decomposition and using ideas from pattern recognition. This method is therefore an adaptive and data driven procedure which segments the data in time-frequency windows using the local cosine transform (LCT). The method was first proposed in [14] and theoretically analyzed in the case of random layered media in [1]. We present its basic steps in Section 3.3. The last method that we call the rank one projection (ROP) filter, is described in Section 3.4. This is a filter that seeks to select the single scattering component of the scattered field. The idea was first developed by Aubry et al. in [2] in the form of the single scattering filter (SSF). ROP is an alternative to SSF, the goal is the same but the procedure for extracting the single scattering component of the data is different and as our numerical results suggest ROP is more efficient than SSF. ROP can

be either applied as an additional filter to the time-frequency windows selected by the LCT-based approach or it can be used together with random matrix theory ideas for selecting the appropriate time-frequency windows. In the latter case, the singular value decomposition of the filtered windowed data is computed and a window is retained when the value of the largest singular value (the singular values are normalized by their quadratic mean) exceeds a certain threshold. Again, it is the value of the threshold that is the critical parameter that determines which windows are selected/rejected. As for the first method the value of the threshold is obtained using statistical properties of the scattered field from the background medium in the absence of reflectors. In this case, the relevant quantity is the statistical distribution of the largest singular value (normalized as mentioned above) of the filtered data. A detailed comparison between the three approaches which summarizes the results of this thesis is presented in [37].

The aim of all these filtering techniques is to enhance the signal to noise ratio of the coherent reflections so as to increase the efficiency and robustness of coherent imaging in strongly scattering media. In order to persuade the reader for the necessity of such filtering, we plot in Figure 3.1 the KM results obtained using the raw data as recorded on the array for the simulation setup shown in Figure 2.1. The images look extremely noisy and unreliable for both the layered and the combined media. In the isotropic clutter, the KM image finds the first reflector but not the second one which is lost in the noise. Our objective is to study the performance of different techniques that enhance the coherent signal received from the reflectors and improve these results.

3.2 KM-based time-frequency window selection

Motivated by the detection criterion based on the peak of the echographic image obtained with focused beamforming (FB) [2, 4], we investigate first how the KM imaging results can be improved by exploiting the knowledge of the incident field in connection with random matrix theory ideas. In this case we need data not only for the total field, but also for the incident field. These can be computed by solving the wave equation as described in Section 2.2 above, for the scattering medium of interest, except that the reflectors are being removed. Note that we do not need the incident field for the exact same realization of the random medium: we can use any realization of the random process μ with the same characteristics, *i.e.*, correlation function and strength of fluctuations.

We decompose the data in time-frequency windows using the LCT window segmentation procedure [18, 30, 14]. It should be noted, that the LCT decomposes the traces in orthonormal bases constructed with smooth time windows modulated

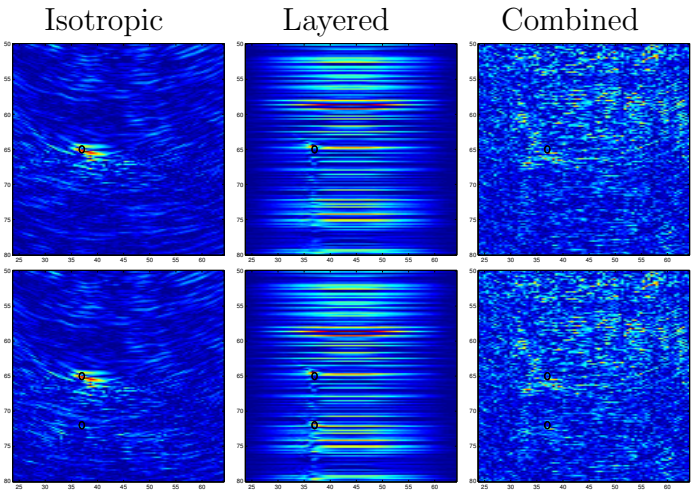

Figure 3.1: KM images for one and two reflectors in strong clutter. From left to right, isotropic, layered and combined medium. Top row: one reflector. Bottom row: Two reflectors. The images are obtained using the raw data as recorded on the array. The scattering media are the ones illustrated in Figure 2.1.

by cosines [18, 30, 14]. The smooth windows avoid the appearance of artificial discontinuities in the transformed signals, which generate large amplitude coefficients at high frequencies. The LCT is efficient for detection and filtering, because we can use the well-established fast algorithms for its implementation [18, 30, 14]. This procedure constructs a binary tree and at each level, l, of the tree the data are decomposed into 2^l windows. The level and window of the tree is chosen adaptively following the algorithm proposed in [14]. We present briefly the main steps of this algorithm in Section 3.3.

Here we prefer to select the level of the tree by fixing the size of the window to the smallest possible, so as to keep all the array data from a hypothetical reflector in our search domain in the same window. For our setup this corresponds to level $l = 4$ and dividing the data in 16 windows. In each window, we compute the Fourier transform of the data and the image I_{KM} for each frequency ω. This means that we construct a set of images $\widetilde{I}_{KM} = \widetilde{I}_{KM}(j, \omega)$ parametrized by the time window j and the frequency ω. It should be noted, that the discretization of the image domain should be selected appropriately so that the value at each pixel is independent. To achieve this we chose a discretization that is of the order of the array resolution, in our case this corresponds to a pixel size $\lambda_0 \times \lambda_0$. We can therefore assume that each image has Q independent coordinates $q = 1, \cdots, Q$ and following [2, 3, 4, 25] we normalize them by their quadratic mean (L_2-norm),

$$\widetilde{I}_{KM}(j,\omega)[q] = \frac{|I_{KM}(j,\omega)[q]|}{\sqrt{\frac{1}{Q}\sum_{q=1}^{Q}|I_{KM}(j,\omega)[q]|^2}}, \quad q = 1,2,...,Q. \tag{3.1}$$

The next step consists in estimating $\rho^{\widetilde{I}_{KM}(\sigma)}$ the image probability density function, by computing a histogram of the normalized images and averaging over all time-frequency couples [2, 3, 4, 25]. From the theoretical point of view, in the case of strong clutter, the normalized image value $\widetilde{I}_{KM}(j,\omega)[q]$ is expected to be the modulus of a gaussian complex random variable with zero mean and variance unity and therefore the corresponding probability density function is given by the Rayleigh law [38, 23],

$$\rho_R(\sigma) = 2\sigma\exp(-\sigma^2). \tag{3.2}$$

However, in practice we prefer to compute the probability density function directly from the data rather than rely on this expression. For the KM image, the variable of interest is the maximum of the image. The distribution function $F^{\widetilde{I}_{max}}(\sigma)$ of the maximum of the image, $\widetilde{I}_{max}(= max\left[\widetilde{I}_{KM}\right])$, is defined by the Q^{th} power of the distribution function $F^{\widetilde{I}_{KM}}(\sigma)$ of its image coordinate, computed by,

$$F^{\widetilde{I}_{KM}}(\sigma) = \int_0^{\sigma} dx\rho^{\widetilde{I}_{KM}}(x). \tag{3.3}$$

In general for a given probability of error γ, a detection threshold can be obtained from,

$$\alpha = F^{-1}(1-\gamma). \tag{3.4}$$

Therefore, given a probability of error γ, we compute a threshold α_{KM} using the distribution function $F^{\widetilde{I}_{max}}(\sigma)$ calculated for the incident field and then we select the windows j and frequencies ω so that,

$$\widetilde{I}_{max}(j,\omega) > \alpha_{\mathrm{KM}}. \tag{3.5}$$

The detection criterion (3.5) suggests that for a given time window j and frequency ω, the reflector is detectable with the given probability of error γ if the maximum of the image at time window j and frequency ω is larger then the threshold α_{KM}. These are the time-frequency couples $(j_\star,\omega_\star)$ that the algorithm selects. Finally, the KM image is built by using the data for the selected time-window(s) $j_\star$ and frequency bandwidth(s) $B_{j_\star}$.

3.3 LCT-based time-frequency window selection

We briefly review here the LCT-based time-frequency window selection algorithm proposed in [14]. The input of the algorithm is the array response matrix $\mathbf{P}(\mathrm{t})$, for

time $t \in [0, T]$ sampled on a mesh with $N_T = 2^m$ points. We also need to specify the maximum level of the tree, $D \leq m$, to be used in the LCT. This is chosen so that we have enough samples of the signal at each level of the tree. The LCT decomposition is performed on a binary tree that has 2^l windows at each level l. For each node (j, l) of the tree, corresponding to window j at tree level l, the local cosine transform of the response matrix is computed.

$$\hat{\mathbf{P}}^l(t_j^l, \omega_n^l) = \left\{ \hat{P}^l(t_j^l, \omega_n^l, \vec{\mathbf{x}}_r, \vec{\mathbf{x}}_s) \right\}_{r,s=1,\ldots,N},$$

with

$$\hat{P}^l(t_j^l, \omega_n^l, \vec{\mathbf{x}}_r, \vec{\mathbf{x}}_s) = \int_0^T dt\, P(t, \vec{\mathbf{x}}_r, \vec{\mathbf{x}}_s) \sqrt{\frac{2}{\Delta t_l}} \chi\left(\frac{t - t_j^l}{\Delta t_l}\right) \cos[\omega_n^l (t - t_j^l)]$$

where

$$t_j^l = j\Delta t_l = \frac{jT}{2^l}, \quad j = 0, 1, \ldots, 2^l \text{ and } \omega_n^l = \frac{\pi\,(n + 1/2)}{\Delta t_l}, \quad n \in \mathcal{N}^l,$$

for frequency indices so that ω_n^l belongs in the available bandwidth B

$$\mathcal{N}^l = \left\{ n = 0, 1, \ldots, N_T/2^l - 1, \;\; \text{s.t.} \;\; \omega_n^l \in B \right\}. \tag{3.6}$$

We show in Figure 3.2 an illustration of the binary tree used in the time-frequency decomposition of the array data. Level $l = 0$ corresponds to one window that contains the data traces over the entire duration of the recording. At level $l = 1$, the data are segmented in two time windows indexed by $j = 0$ and $j = 1$. At level $l = 2$, the data are segmented in four time windows indexed by $j = 0, 1, 2$ and 3, etc.

The detection criterion of the algorithm in [14] relies on the singular value decomposition of the local cosine matrices of coefficients. For each l and t_j^l we compute the SVD of $\hat{\mathbf{P}}^l(t_j^l, \omega_n^l)$, frequency by frequency. Let us denote by $\sigma_q^{l,j}(\omega_n^l)$ the singular values, for $q = 1, ..., N$. We then form the matrices of the first N_{SV} normalized singular values,

$$S^{l,j} = \left\{ \tilde{\sigma}_q^{l,j}(\omega_n^l) \right\}_{1 \leq q \leq N_{SV},\, n \in \mathcal{N}_S^l}, \quad \text{where} \;\; \tilde{\sigma}_q^{l,j}(\omega_n^l) = \frac{\sigma_q^{l,j}(\omega_n^l)}{\max_{n'} \sigma_q^{l,j}(\omega_{n'}^l)} \tag{3.7}$$

over the restricted set of frequency indices

$$\mathcal{N}_S^l = \left\{ n = 0, 1, \ldots, N_T/2^l - 1, \;\; \text{s.t.} \;\; \omega_n^l \in B_S \right\}.$$

The number of the singular values N_{SV} and the selected frequency bandwidth B_S depend on the data and have to be chosen appropriately. Typically we should have

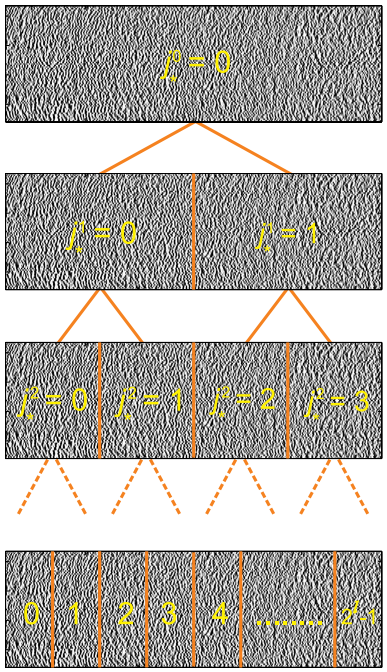

Figure 3.2: Illustration of the time windowing segmentations of the array data traces at different tree levels indexed by l.

$2M \leq N_{SV} \leq N$ with M the number of scatterers we are searching for, and N the dimension of the response matrix. The bandwidth B_S is the part of the frequency spectrum on which the scatterers are detectable. This depends on the clutter and is very different, for example, in isotropic and finely layered random media, but we do not need to know it in advance, it can be determined directly from the data.

The algorithm next adaptively selects the level of the tree and the windows that contain coherent echoes. The distinction is based on a break of a pattern recognition idea that is carried out as follows. Compute the first two singular values of the matrices $S^{l,j}$ and form their ratio,

$$\lambda^{l,j} = \gamma_2^{l,j}/\gamma_1^{l,j}, \tag{3.8}$$

$\gamma_q^{l,j}$, $q = 1, 2$, being the first and the second singular values of $S^{l,j}$, respectively. At each level l, the window that contains the coherent echoes is selected by looking at the maxima of $\lambda^{l,j}$. Adaptive refinement until the finest tree level at which the maximum persists is performed, and the optimal couples $(j^\star, l^\star)$ are determined. Finally the array data are filtered by zeroing the LCT coefficients in all other windows that have not been selected and by projecting the LCT matrix on the subspace corresponding to the top singular values in the selected windows. The algorithm's output is the filtered response matrix that will be denoted here $\mathbf{P}^{LCT}$. More information about the adaptive LCT-based filtering algorithm can be found in [14].

3.4 Rank One Projection (ROP) filter

In this section we describe a filtering algorithm that aims at separating the single scattered echoes of the reflectors from the multiple scattered field from the background. This algorithm has been proposed in [15] and is an alternative to the SSF filter of Aubry et al. [2, 3]. We do not consider here the direction of arrival selection proposed in [15], and focus only on the first three steps of the algorithm described in Section 4.2 of [15]. These are the following: Given the data $\mathbf{P}_o(t)$ filtered in a time window of interest centered at time t_o, selected for example with the LCT-based algorithm described in the previous section, we first compute the Fourier transform of the data,

$$\widehat{\mathbf{P}}_o(\omega) = \int_{-\infty}^{\infty} \mathbf{P}_o(t) e^{i\omega t} dt.$$

Then we back-propagate the data to a test point $\vec{\mathbf{y}}_o = (0, L_o)$ located at the range $L_o = t_o/(2c_0)$, c_0 being the smooth part of the velocity assumed here to be constant. This step is performed so as to remove the fast oscillatory phase from the data corresponding to the range difference between the array and the reflector,

$$\widehat{P}^{\mathrm{BP}}(\omega,\vec{\mathbf{x}}_r,\vec{\mathbf{x}}_s)=\widehat{P}_o(\omega,\vec{\mathbf{x}}_r,\vec{\mathbf{x}}_s)e^{-i\omega(\tau(\vec{\mathbf{y}}_o,\vec{\mathbf{x}}_s)+\tau(\vec{\mathbf{x}}_r,\vec{\mathbf{y}}_o))}.$$

Here $\tau(\vec{\mathbf{x}},\vec{\mathbf{y}})$ denotes the travel time between points $\vec{\mathbf{x}}$ and $\vec{\mathbf{y}}$, which in the case of a constant velocity c_0 is simply the distance between the two points divided by the velocity.

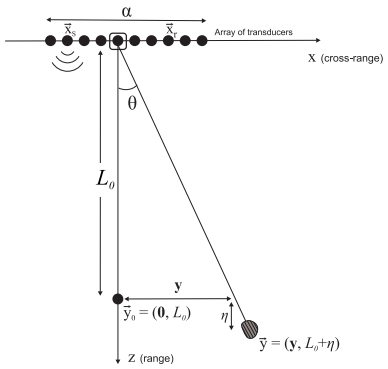

Figure 3.3: Array imaging illustration of a reflector located at $\vec{\mathbf{y}}=(\mathbf{y},L_o+\eta)$. $\vec{\mathbf{x}}_s$ is a source and $\vec{\mathbf{x}}_r$ is a receiver on the array. The point $\vec{\mathbf{y}}_o=(\mathbf{0},L_o)$ denotes the test point at which we back-propagate the data. The array aperture a is small compared to the range L_o.

Assuming the reflector is far enough from the array and in a small cross-range distance from the array center, so that the paraxial approximation is valid, the phase of the back-propagated response matrix corresponding to a reflector located at $\vec{\mathbf{y}}=(\mathbf{y},L_o+\eta)$ which is at the vicinity of $\vec{\mathbf{y}}_o$ (see Figure 3.3 for a schematic) reduces to

$$\frac{\omega}{c_0}\left(2\eta+\frac{|\mathbf{y}|^2}{L_o}-\frac{(\vec{\mathbf{x}}_r+\vec{\mathbf{x}}_s)\cdot\mathbf{y}}{L_o}\right) \tag{3.9}$$

and is independent of the difference $\vec{\mathbf{x}}_r-\vec{\mathbf{x}}_s$.

Exploiting this remark, the next step of ROP consists in rotating the back-propagated data by 90 degrees. This corresponds to a change of variables from $(\vec{\mathbf{x}}_s,\vec{\mathbf{x}}_r)$ to $(\bar{\mathbf{x}}_{\mathrm{rs}},\tilde{\mathbf{x}}_{\mathrm{rs}})$ defined by $\bar{\mathbf{x}}_{\mathrm{rs}}=\frac{\vec{\mathbf{x}}_s+\vec{\mathbf{x}}_r}{2}$ and $\tilde{\mathbf{x}}_{\mathrm{rs}}=\vec{\mathbf{x}}_r-\vec{\mathbf{x}}_s$. For an array with N elements, the rotated matrix has dimensions $(2N-1)\times(2N-1)$ and is zero outside a rhombus structure. If we denote $\mathrm{KK}=\widehat{P}^{\mathrm{BP}}(\omega,:,:)$ we define the rotated matrix KR as

$$\mathrm{KR[i+j-1,i-j-(1-N)+1]=KK[i,j],}\quad\forall \mathrm{i}=1,\ldots,\mathrm{N,j}=1,\ldots,\mathrm{N.}$$

Recalling now (3.9), since the phase of the coherent part of $\widehat{P}^{\mathrm{BP}}$ is independent of $\tilde{\mathbf{x}}_{\mathrm{rs}}$, the matrix KR should be independent of its column index. This is what the

ROP filter enforces by averaging over $\tilde{\mathbf{x}}_{\rm rs}$ the rotated matrix,

$$\mathrm{KA[i,j]} = \frac{1}{\mathrm{n[i]}} \sum_{\mathrm{k}} \mathrm{KR[i,k]}, \quad \forall \mathrm{i} = 1, \ldots, 2\mathrm{N}-1, \mathrm{j} = 1, \ldots, 2\mathrm{N}-1$$

where $n[i]$ is the number of non-zero elements of the i-th row of the matrix KR precomputed in advance. The matrix KA computed as described above is the matrix with identical columns that best approximates KR with respect to the Frobenius norm, taken in the space of matrices with the same rhombus support as KR (see also Section 4.2 in [15]). The next step of ROP consists in rotating back the matrix to its physical coordinates and by removing the zero elements introduced during the rotation step. Let us denote $\widehat{P}^{\rm f}(\omega, :, :)$ the resulting matrix of dimensions $N \times N$ (for each frequency).

The last step of the ROP filter is undoing the back-propagation to the test point $\vec{\mathbf{y}}_o$,

$$\widehat{P}^{\rm ROP}(\omega, \vec{\mathbf{x}}_r, \vec{\mathbf{x}}_s) = \widehat{P}^{\rm f}(\omega, \vec{\mathbf{x}}_r, \vec{\mathbf{x}}_s) e^{+i\omega(\tau(\vec{\mathbf{y}}_o, \vec{\mathbf{x}}_s) + \tau(\vec{\mathbf{x}}_r, \vec{\mathbf{y}}_o))}.$$

As mentioned above the ROP filter can be viewed as an alternative of the SSF filter [2]. The difference between the two filters is in the way the rotation and projection steps are performed, while both ROP and SSF exploit the same idea that the coherent reflected field should be independent of the difference variable $\tilde{\mathbf{x}}_{\rm rs}$. In connection to random matrix theory, and assuming knowledge of the incident field, ROP can be used for selecting the time-frequency windows at which the reflectors are detectable. The approach is similar to the one described in [2], and we review it in the next section. Alternatively ROP can be applied just as an additional filter after selecting the time-frequency windows with the LCT-based algorithm presented in Section 3.3. We will call this approach LCT+ROP.

3.5 ROP-DORT based time-frequency window selection

The idea is to decompose the data in time-frequency windows, apply the ROP filter for each window and frequency, and base the selection on whether the largest singular value of the filtered response matrix is above a certain threshold determined using the data for the incident field. Therefore, as in Section 3.2, we assume the incident field is known, and we decompose the data in time windows by selecting the size of the window to be the smallest possible so as to keep all the array data from a hypothetical reflector in the search domain inside the same window. For our setup this corresponds to level $l = 4$ and dividing the data in $N_l = 16$

windows. We denote Δt the window size and assuming that the data are available in the time window $[t_{\text{begin}}, t_{\text{end}}]$, we define T_j, as

$$T_j = t_{\text{begin}} + (j-1)\Delta T \quad \text{for} \quad j = 1, \ldots, N_l.$$

The central time for each window is $T_{j+1/2} = \frac{T_j + T_{j+1}}{2}$, $j = 1, \ldots, N_l$. For the incident field, we compute, for the data restricted in each window $j = 1, \ldots, N_l$, the SVD of the filtered by ROP response matrix, frequency by frequency. The ROP filter is applied as descibed in the previous section and the only parameter that is changing is the test point $\vec{\mathbf{y}}_o^j$ that depends on the window j, $\vec{\mathbf{y}}_o^j = (\mathbf{0}, L_{j+1/2})$ with $L_{j+1/2} = \frac{c_0}{2} T_{j+1/2}$.

Denoting by N_f the number of frequencies we have $N_l \times N_f \times N$ singular values $\sigma_q^j(\omega_n)$, $j = 1, \ldots, N_l$, $n = 1, \ldots, N_f$ and $q = 1, \ldots, N$. Then the singular values, at each window j and frequency ω_n, are normalized by their quadratic mean,

$$\widetilde{\sigma}_q^j(\omega_n) = \frac{\sigma_q^j(\omega_n)}{\sqrt{\frac{1}{N}\sum_{p=1}^{N} (\sigma_p^j(\omega_n))^2}}. \tag{3.10}$$

and the first singular value, denoted $\sigma_1^{\text{ROP}}(j, \omega_n)$ is obtained. Given a probability of error γ we estimate the threshold α^{ROP} from the primitive $F_1^{\text{ROP}}(\sigma)$ of $\rho_1^{\text{ROP}}(\sigma)$, the probability density function of the largest singular value σ_1^{ROP}. This is the first important step. Next using this threshold, we can select the time-frequency windows of interest by choosing the couples (j, ω_n) for which the largest singular value of the filtered by ROP data for the total field is above this threshold.
For the total field, we compute, in the same way as for the incident field, the filtered response matrix and its first singular value as a function of frequency ω_n and window j. We denote this as $\sigma_1^{\text{total}}(j, \omega_n)$. Using the threshold α^{ROP} computed, we chose the windows j and frequencies ω_n for which

$$\sigma_1^{\text{total}}(j, \omega_n) > \alpha^{\text{ROP}} \tag{3.11}$$

The result is the selection of one (or more) time windows and a corresponding frequency range of interest. The final image is computed using the filtered data in the selected window(s) and frequency range after applying DORT [34, 35], that is after projecting the filtered data on the subspace corresponding to the largest singular value. We will call this approach ROP+DORT and compare it with the LCT+ROP approach in the next chapter.

Chapter 4

Numerical results

4.1 Overview

In this chapter we compare how the different time-frequency selection procedures described in the previous chapter perform using our simulated data.

4.2 Results with the KM-based time-frequency window selection

We start with the KM-based time-frequency window selection procedure. The estimator $\rho^{\widetilde{I}_{KM}}(\sigma)$ of the image probability density function compared to the Rayleigh law $\rho_R(\sigma)$, is displayed in Figure 4.1.

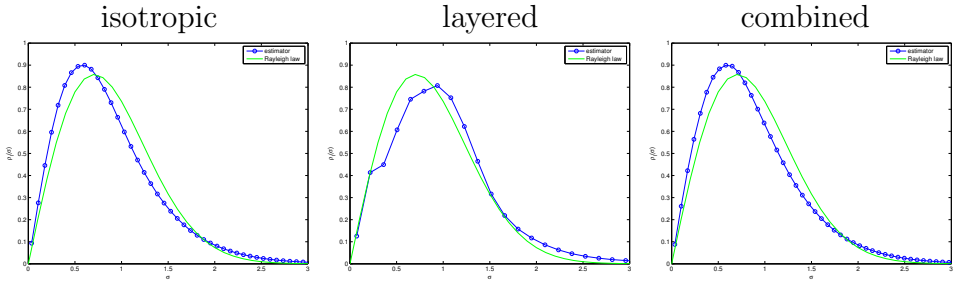

Figure 4.1: The estimator $\rho^{\widetilde{I}_{KM}}(\sigma)$ (blue) of the image the probability density function is compared with the Rayleigh law (light green) for the three cluttered media.

For a probability of error $\gamma = 0.001$ (we will use this value throughout the dissertation), the corresponding numerical values of the detection threshold are

summarized in Table 4.2.

Isotropic	Layered	Combined
$\alpha = 9.1$	$\alpha = 16.0$	$\alpha = 11.8$

Table 4.1: Summary table of detection thresholds for the KM-based time frequency window selection.

After calculating the detection thresholds, we can go further and perform the KM-based detection test in order to select the time-frequency windows of interest. We first consider the data for one reflector. The detection criterion of eq. (3.5) provides, after application of the detection thresholds indicated in Table 4.2, that the target can be detected at the selected time-windows $j_\star$ and frequency ranges $B_{j_\star}$ shown in Table 4.2.

Medium	Detection criterion	Selected windows	Selected bandwidths
Isotropic	$\widetilde{I}_{max}(j,\omega) > 9.1$	$j_\star = 7, 8$	$B_7 = [1.7, 6.6]$ MHz $B_8 = [1.7, 10.0]$ MHz
Layered	$\widetilde{I}_{max}(j,\omega) > 16.0$	$j_\star = 6, 7$	$B_6 = [1.7, 3.2]$ MHz $B_7 = [1.7, 3.9]$ MHz
Combined	$\widetilde{I}_{max}(j,\omega) > 11.8$	$j_\star = 7, 8$	$B_7 = [1.7, 5.9]$ MHz $B_8 = [1.6, 5.9]$ MHz

Table 4.2: One reflector: Summary table of selected windows and bandwidths, based on the KM detection criterion.

We remark that the bandwidths selected do not contain the lower part of the frequency spectrum below 1.5MHz and are confined below the central frequency of 10MHz. Especially for the layered medium, the selected frequencies are below 4MHz. This is in agreement with the theory that suggests that in layered clutter only the lower frequencies can penetrate deep enough in the medium and see the reflector. The amplitude of the coherent field decays exponentially with ω^2 and therefore the higher frequencies cannot be used for imaging [1].

We next compute the KM images obtained by using the selected windows and bandwidths depicted in Table 4.2. The results are significantly better than the KM images obtained with the raw data shown in Figure 3.1. We next consider the case of two reflectors. The selected time-frequency windows are given in Table 4.2. The corresponding images are shown in Figure 4.3. The results are not very good: This method does not succeed in selecting only the windows that contain echoes from the reflectors and although the first reflector can be successfully imaged, the

second one is lost in the noisy reverberations. As we will see next, better results can be obtained with the other two time-frequency window selection methodologies.

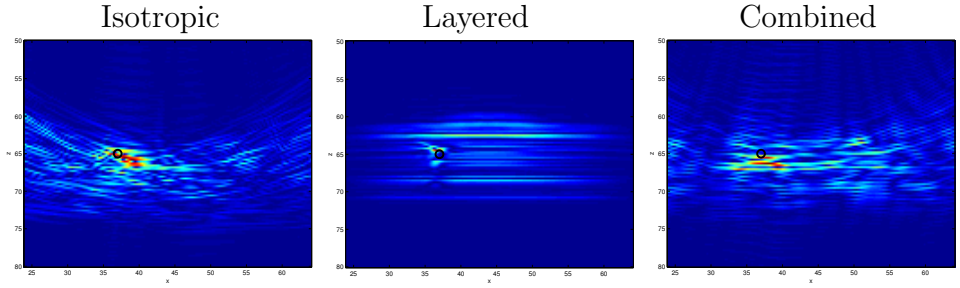

Figure 4.2: One reflector case. KM images obtained by using the selected windows and bandwidths depicted in Table 4.2.

Medium	Detection criterion	Selected windows	Selected bandwidths
Isotropic	$\widetilde{I}_{max}(j,\omega) > 9.1$	$j_\star = 7, 8, 9, 10$	$B_7 = [1.7, 6.6]$ MHz $B_8 = [1.7, 11.4]$ MHz $B_9 = [1.7, 11.7]$ MHz $B_{10} = [1.7, 8.8]$ MHz
Layered	$\widetilde{I}_{max}(j,\omega) > 16.0$	$j_\star = 6, 7, 8$	$B_6 = [1.7, 3.2]$ MHz $B_7 = [1.7, 3.4]$ MHz $B_8 = [1.7, 3.5]$ MHz
Combined	$\widetilde{I}_{max}(j,\omega) > 11.8$	$j_\star = 7, 8, 9$	$B_7 = [1.7, 6.0]$ MHz $B_8 = [1.7, 6.0]$ MHz $B_9 = [1.6, 6.0]$ MHz

Table 4.3: Two reflectors: Summary table of selected windows and bandwidths, based on the KM detection criterion.

4.3 Results using the ROP filter

We compare here the results obtained using the ROP filter either combined with random matrix theory and DORT, or with the LCT-based methodology for selecting the time-frequency windows that contain the coherent echoes from the reflectors that we wish to image. We also show in the one reflector case the results obtained by the SSF approach which is less efficient due to the fact that half of the array data is disregarded (the results are similar for the two reflectors).

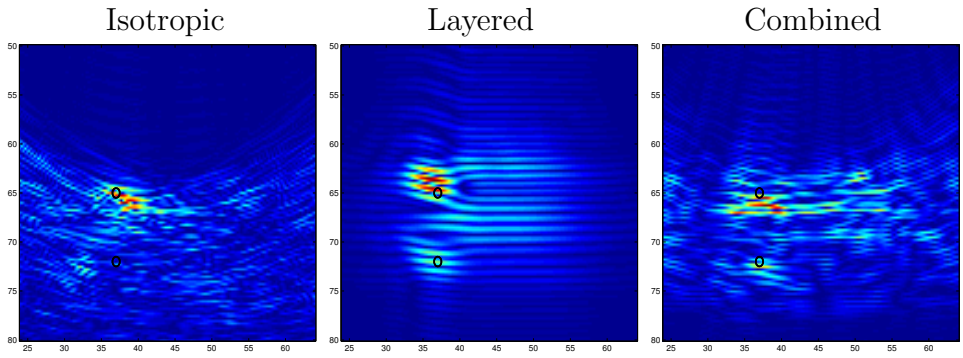

Figure 4.3: Two reflectors case. KM images obtained by using the selected windows and bandwidths reported in Table 4.2.

We will first compute the probability density function $\rho^{\mathrm{ROP}}(\sigma)$ of the singular values of the filtered response matrix. To do so we use the histogram $\mathcal{H}(\sigma)$, computed as follows: The bins of the histogram are the intervals $[m\ w, (m+1)w]$, with w the width of the bin and m non-negative integers. The value of $\mathcal{H}(\sigma)$ is the number of normalized singular values $\widetilde{\sigma}_q^j(\omega_n)$ contained in the same bin as σ, for all time window indices $j = 1, \ldots, N_l$, the N_f frequency indices $n = 1, \ldots, N_f$, and the N singular value indices $q = 1, \ldots, N$. Consequently, the estimator of the probability density function of the singular values is given by

$$\widehat{\rho}_{\mathrm{ROP}}(\sigma) = \frac{\mathcal{H}(\sigma)}{w N_f\ N_l\ N} \tag{4.1}$$

We show in Figure 4.4, the estimators $\widehat{\rho}_{ROP}(\sigma)$ for the filtered data after keeping only one element in four of the filtered matrix so as to remove residual correlations in the data. The filtered matrix is expected to be a random Hankel matrix and therefore we compare the estimators to the Hankel law, $\rho_H(\sigma)$ [17], *i.e.*, the probability density function of Hankel matrices of the same size as our matrix. The estimation of the Hankel law $\rho_H(\sigma)$ is performed numerically since up to now no analytical expression has been recorded in the literature. As we can see, the agreement between the theory and the experiments is almost perfect for the isotropic and the combined medium (recall that we have kept only one out of four elements of the filtered response matrix). In the layered case, the invariance in the cross-range direction of the medium yields a Toeplitz matrix $\mathbf{P}(\mathrm{t})$ characterized by persistent correlations [14]. That is why on the right plot of Figure 4.4, the experimental distribution of the singular values of the filtered data for the layered medium is compared to the filtered Toeplitz law $\rho_T(\sigma)$ [17, 32]. The distribution of singular values of a filtered random Toeplitz matrix is also generated numerically. As we observe in the right plot in Figure 4.4, the agreement between the two curves is quite satisfactory, except the region of values where $\sigma < 0.5$.

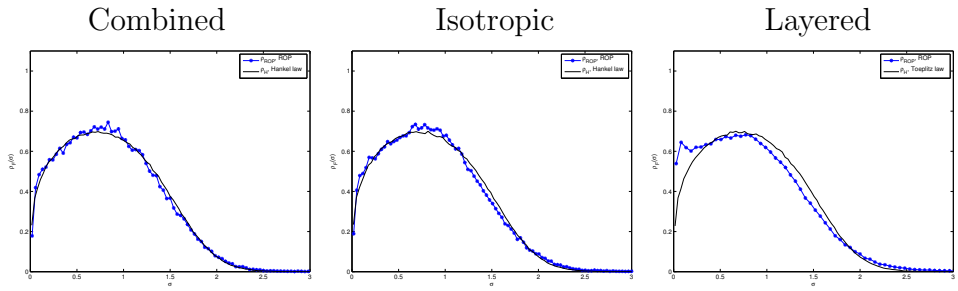

Figure 4.4: (Incident Field): Estimators $\widehat{\rho}_{ROP}(\sigma)$ are compared to the theoretical curves (black curves). On the left and center plots, the blue curves correspond to the estimators computed after keeping only one element in four of the filtered matrix (to remove residual correlations in the data), are compared to the Hankel law $\rho_H(\sigma)$ (black curve). On the right plot the corresponding estimator $\widehat{\rho}_{ROP}(\sigma)$ is compared to the Toeplitz distribution law $\rho_T(\sigma)$ (black curve).

We show in Figure 4.5 the distribution functions $F_1^{ROP}(\sigma)$ for the three cluttered media. The detection thresholds are represented with red vertical lines where the admitted probability error γ has been set to 0.001. The corresponding numerical values of the detection thresholds for the ROP method, are summarized in Table 4.3.

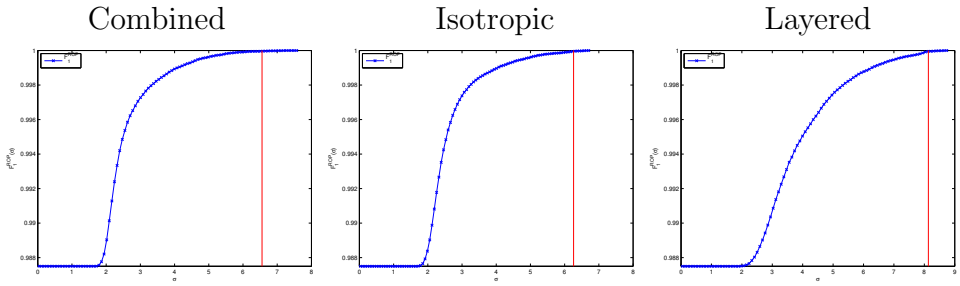

Figure 4.5: (Incident Field). The distribution functions $F_1^{ROP}(\sigma)$ (blue curves), obtained for the three different media. The red vertical lines represent the detection thresholds α^{ROP} shown on Table 4.3, for a probability of error $\gamma = 0.001$.

In Table 4.3, the detection thresholds for the SSF technique, are also presented. Recall that the response matrix filtered by SSF is of dimension $N = 39$ because of half of the data is disregarded through the SSF rotation procedure.

After calculating the detection thresholds, we can go further and select the time-frequency windows for which the reflectors are detectable. The results for the combined medium are given in Tables 4.3 and 4.3, respectively, for both the ROP and the SSF techniques.

Scattering medium	Combined	Isotropic	Layered
Detection threshold	$\alpha^{\text{ROP}} = 6.6$	$\alpha^{\text{ROP}} = 6.3$	$\alpha^{\text{ROP}} = 8.1$

Table 4.4: (Incident Field): Summary table of detection thresholds for the ROP filter.

Scattering medium	Combined	Isotropic	Layered
Detection threshold	$\alpha^{\text{SSF}} = 5.5$	$\alpha^{\text{SSF}} = 5.1$	$\alpha^{\text{SSF}} = 5.3$

Table 4.5: (Incident Field): Summary table of detection thresholds for the SSF filter.

Medium	Detection criterion	Selected windows	Selected bandwidths
Combined	$\sigma_1^{\text{total}}(j, \omega_n) > 6.6$	$j_\star^4 = 7, 8$	$B_7 = [1.8, 8.1]$ MHz $B_8 = [1.8, 8.1]$ MHz
Isotropic	$\sigma_1^{\text{total}}(j, \omega_n) > 6.3$	$j_\star^4 = 7, 8$	$B_7 = [1.7, 7.6]$ MHz $B_8 = [2.3, 7.4]$ MHz
Layered	$\sigma_1^{\text{total}}(j, \omega_n) > 8.1$	$j_\star^4 = 6, 7$	$B_6 = [1.4, 3.3]$ MHz $B_7 = [1.4, 3.5]$ MHz

Table 4.6: One reflector: Summary table of the selected windows and bandwidths, based on the detection criterion of ROP combined with DORT.

Medium	Detection criterion	Selected windows	Selected bandwidths
Combined	$\sigma_1^{\text{total}}(j, \omega_n) > 5.5$	$j_\star^4 = 7, 8$	$B_7 = [1.6, 6.0]$ MHz $B_8 = [1.7, 6.0]$ MHz
Isotropic	$\sigma_1^{\text{total}}(j, \omega_n) > 5.1$	$j_\star^4 = 7, 8$	$B_7 = [1.8, 6.1]$ MHz $B_8 = [1.9, 5.8]$ MHz
Layered	$\sigma_1^{\text{total}}(j, \omega_n) > 5.3$	$j_\star^4 = 6, 7$	$B_6 = [1.2, 3.2]$ MHz $B_7 = [1.2, 3.2]$ MHz

Table 4.7: One reflector: Summary table of the selected windows and bandwidths, based on the detection criterion of SSF.

At the top row of Figure 4.6, we present the KM images obtained using the SSF filter at the selected windows and bandwidths shown on Table 4.3, while at the bottom row the KM images obtained using the ROP filter combined with DORT at the selected windows and bandwidths shown on Table 4.3, are illustrated. We

observe that the results provided by the SSF approach are less precise and more noisy.

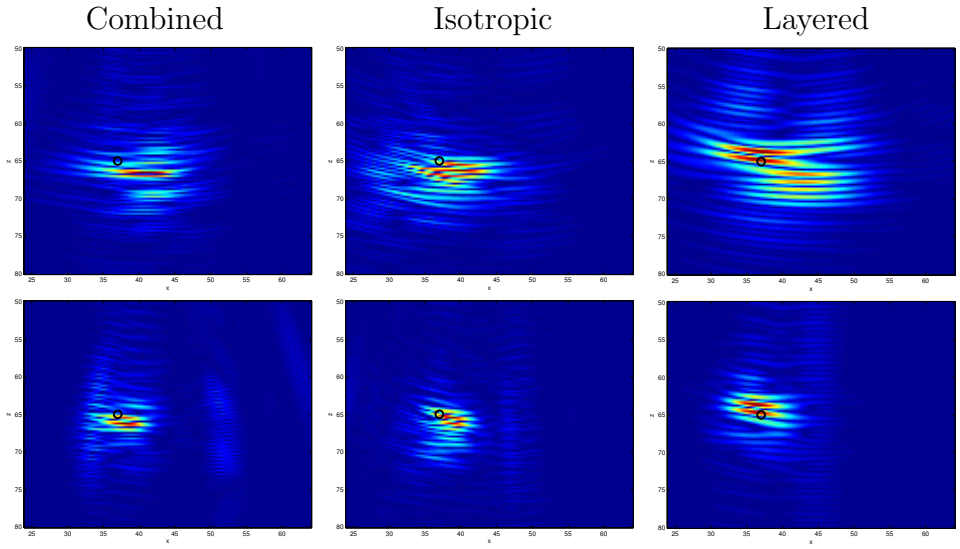

Figure 4.6: (Total Field). **Top** : The KM images obtained using the SSF filter at the selected windows and bandwidths shown on Table 4.3 **Bottom** : The KM images obtained using the ROP filter combined with DORT at the selected windows and bandwidths shown on Table 4.3.

It should be noted here, that the LCT selection algorithm is based on the behavior of the larger singular values of the LCT of the response matrix $\mathbf{P}(t)$, across frequencies. In particular, we seek to identify a break in the pattern among the singular values as they vary over frequency. The idea is that, if only echoes from the cluttered background medium are present in a window, the larger singular values of the LCT in this window should all look alike and have a similar behavior across frequencies [14]. On the other hand, we expect at least one singular value with different behavior when echoes from a detectable object are present in the time window.

We plot in Figure 4.7 the singular values in three windows at level $l = 4$. Starting with the window indexed by $j = 5$, we note that the singular values remain tightly clustered (especially in the lower part of the bandwidth below 5Hz), until we reach the index $j = 7$. This is the window that contains the coherent echoes from the reflector, and it is distinguished from the others by an anomalous singular value (here we observe two) at the lower frequencies. This anomaly in the behavior also appears for the other cluttered media considered in our simulations. The frequency range over which the coherent echoes are detectable depends on the characteristics of the background medium. In the layered case the reflector can be detected only for the lower frequencies because higher frequencies are strongly

attenuated by scattering as shown in [1]. A similar behavior is observed in the combined medium while in the isotropic clutter the reflectors are detectable across the whole frequency bandwidth (see Figure 4.10).

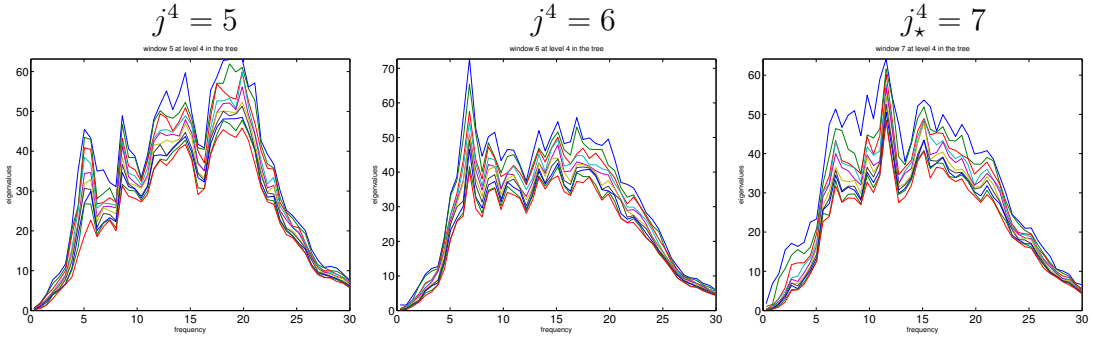

Figure 4.7: Combined medium. The top 10 singular values as functions of frequency. We illustrate the time windows at level 4 indexed by $j = 5, 6, 7$. Each eigenvalue is plotted with a different color.

On the left plot of Figure 4.8, the LCT selection criterion (see Section 3.3, [14]) for the combined medium, is depicted. It suggests that we have one reflector located at window 7, at level 4 of the binary tree. The plot has a clear local maximum in the desired time window of the reflector. On the right plot, we illustrate the behavior of the top 10 singular values as a function of the frequency in the selected time-window. We observe an anomalous behavior for the first singular value (probably the second one), at the lower frequencies. The selected frequency bandwidth is $B = [0, 4.8]$ MHz.

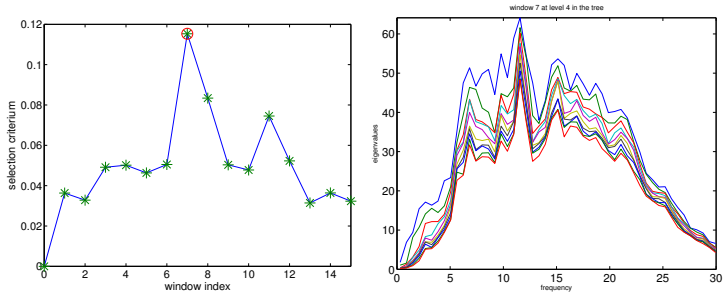

Figure 4.8: Combined medium. On the left, we see the LCT selection criterion $\lambda^{4,j}$ as function of the window index $j = 0, ..., 2^4 - 1$. On the right we see the top 10 singular values with respect to the frequency in the selected window 7.

The imaging results using the different approaches in the combined medium are summarized in Figure 4.9. We observe that the LCT+ROP image is less noisy

in the cross-range direction compared to the LCT image. We also find the image produced by LCT+ROP better than the ROP+DORT image. Similar results have been obtained for other realizations of the combined cluttered medium.

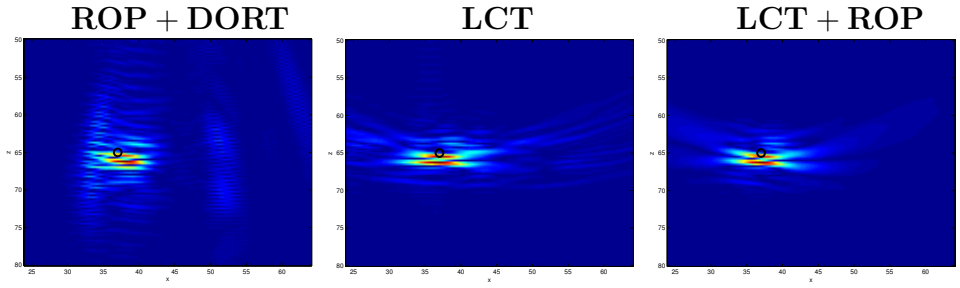

Figure 4.9: Combined medium (Total Field). Left: The KM image of the data obtained using the ROP filter combined with DORT at the selected windows and bandwidths shown on Table 4.3. Middle: The KM image obtained using the data at the selected window and bandwidth provided by the LCT-based algorithm, $j_\star^4 = 7$ and $B = [0, 4.8]$ MHz. Right: ROP filter is combined with LCT.

We next present results for isotropic and layered clutter. In the isotropic regime, the RMT-based detection test of eq. (3.11) for the known detection threshold calculated in Table 4.3, suggests that the reflector can be detected at windows $j_\star^4 = 7, 8$ and bandwidths $B_7 = [1.7, 7.6]$MHz and $B_8 = [2.3, 7.4]$MHz, respectively, as indicated in Table 4.3. The LCT-based detection criterion of eq. (3.8) for the isotropic medium, is illustrated on the left plot of Figure 4.10. It indicates that we have one reflector located at window 7 and at level 4 in the tree. The plot has a clear maximum in the desired time window that contains the reflector's echoes. On the right plot, we investigate the behavior of the top 10 singular values with respect to frequency for the selected window and level. We observe that the first two singular values are detached from the rest for the whole frequency range. This result permits us to keep the entire frequency band $B = [0, 30]$ MHz.

The migration images for the isotropic medium that have been obtained using the selected windows and bandwidths are depicted in Figure 4.11. We show on the left plot, the image obtained after the application of the ROP method combined with DORT at the desired time-windows $j_\star^l$ and bandwidths $B_{j_\star^l}$, summarized in Table 4.3. In the middle plot, the image is produced while using the time-frequency LCT-based filtering technique for the selected window 7 and bandwidth $B = [0, 30]$MHz. We observe that the image is noisy and several maxima appear close to the true position of the reflector due to the residual multiple scattering on the filtered data. However, the additional action of the ROP filter significantly improves the image by removing the multiple scattering contribution from the filtered data, as shown on the right image of Figure 4.11. What is also surprising,

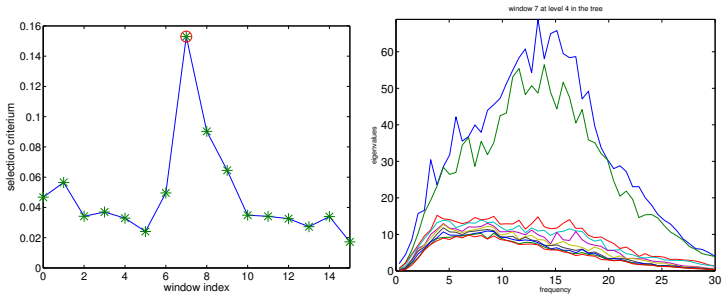

Figure 4.10: Isotropic medium. On the left, we see the LCT selection criterion $\lambda^{4,j}$ as function of the window index $j = 0, ..., 2^4 - 1$. On the right we see the top 10 singular values with respect to the frequency in the selected window 7.

is that the RMT-based detection leads to a significantly smaller bandwidth $\approx [2, 7]$MHz that is used for the image on the left, which explains the worse range resolution obtained in this case. The combination of LCT with ROP gives the best results.

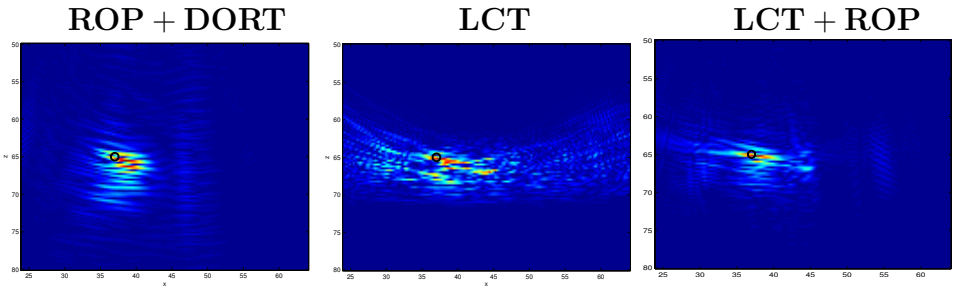

Figure 4.11: Isotropic medium (Total Field). From left to right: The KM image of the data while using the ROP filter combined with DORT at the selected windows and bandwidths shown on Table 4.3, LCT and LCT+ROP image using $j_\star^4 = 7$ and $B = [0, 30]$MHz.

For the layered clutter case, the detection threshold for ROP is calculated on the right column of Table 4.3. For the given threshold, the detection criterion described by eq. (3.11) is performed and selects the windows and bandwidths summarized on Table 4.3, for which the target is detectable within a layered back-scattering regime.

The LCT detection test is performed for the layered medium. The left plot of Figure 4.12 suggests that we have one target located at window 6, at level 4. On the right plot we show the behavior of the top 10 singular values as function of the frequency in the selected time-window. We observe an anomalous behavior of the first singular value (arguably two) only at the lower frequencies $B = [0, 3]$MHz.

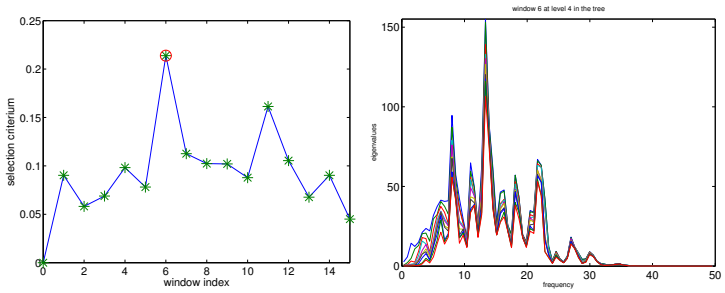

Figure 4.12: Layered medium. On the left, we see the LCT selection criterion $\lambda^{4,j}$ as function of the window index $j = 0, ..., 2^4 - 1$. On the right we see the top 10 singular values with respect to the frequency in the selected window 6.

In Figure 4.13 we display the imaging results for ROP+DORT, LCT and LCT+ROP. The bandwidths selected in this case by the two approaches are similar, although the RMT-based criterion does not include the frequencies below 1.5MHz. We observe that the combination LCT+ROP gives again the best image.

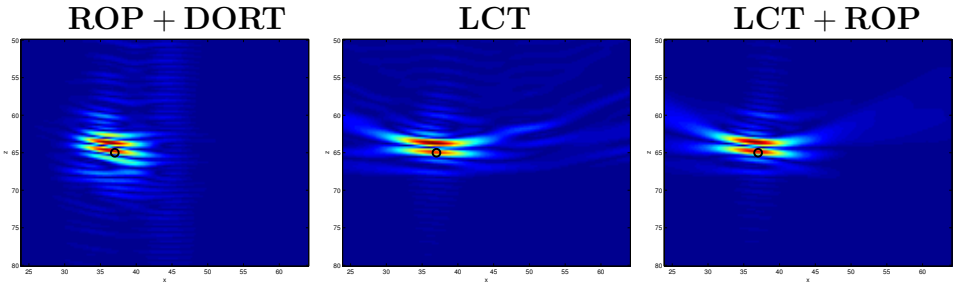

Figure 4.13: Layered medium (Total Field). From left to right: The KM image of data while using the ROP filter combined with DORT at the selected windows and bandwidths shown on Table 4.3, LCT and LCT+ROP using $j_\star^4 = 6$ and $B = [0, 3]$MHz.

We finally present results for the two reflectors' case. First for the combined medium, we give the selected windows and bandwidths by the RMT-criterion in Table 4.3.

In Figure 4.14 the LCT selection criterion of eq. (3.8) for the combined medium, is illustrated. It suggests that we have two targets, one located at window 7 and one at window 9. On the center and right plots we observe the behavior of the top 10 singular values as function of the frequency in the selected time-windows. In both plots, we observe an anomaly for the first singular value (probably two) at the lower frequencies for $B = [0, 4.8]$ MHz. This is the same bandwidth as the one selected for the one reflector case (see Figure 4.9).

Medium	Detection criterion	Selected windows	Selected bandwidths
Combined	$\sigma_1^{\text{total}}(j,f) > 6.6$	$j_\star^4 = 7,8,9$	$B_7 = [1.8, 8.1]$ MHz $B_8 = [1.8, 8.0]$ MHz $B_9 = [1.8, 7.4]$ MHz
Isotropic	$\sigma_1^{\text{total}}(j,f) > 6.3$	$j_\star^4 = 7,8,9,10$	$B_7 = [1.7, 7.6]$ MHz, $B_8 = [2.3, 7.4]$ MHz $B_9 = [2.0, 6.9]$ MHz $B_{10} = [2.2, 7.4]$ MHz
Layered	$\sigma_1^{\text{total}}(j,f) > 8.1$	$j_\star^4 = 6,7,8$	$B_6 = [2.2, 3.2]$ MHz $B_7 = [1.9, 3.27]$ MHz $B_8 = [2.0, 3.64]$ MHz

Table 4.8: Two reflectors: Summary table of the selected windows and bandwidths, based on the detection criterion of ROP combined with DORT.

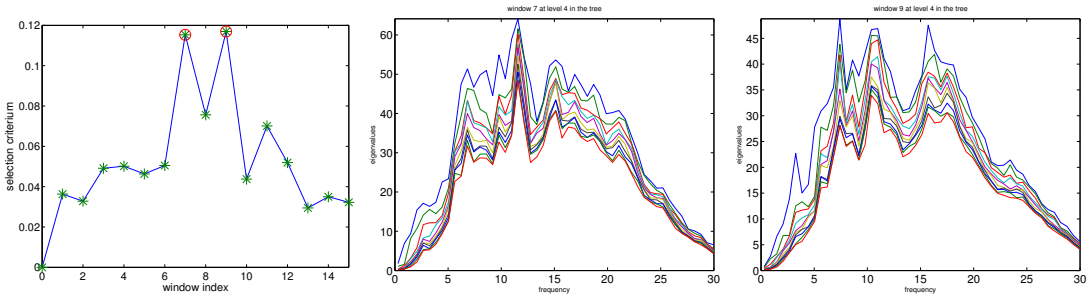

Figure 4.14: Combined medium. On the left we plot the selection criterion that suggests that we have two targets one located at window 7 and one at window 9. On the center and right plots we plot the singular values in the selected windows 7 and 9, respectively.

In the top row of Figure 4.15, the left and center images are obtained by applying the LCT-based filtering procedure in the selected time-windows and frequency range. Indeed, we clearly detect the first reflector at time-window $j_\star^4 = 7$ and the second one at $j_\star^4 = 9$. The application of the ROP filter combined with DORT to the data at the desired time-windows $j_\star^4 = 7, 8, 9$, is shown on the right. We observe that the ROP filter combined with DORT provides a better focusing around the correct positions of the reflectors in both range and cross-range direction compared to the LCT-based filter. However, the image for the second target is weak and this has nothing to do with the quality of the detection criterion but is rather due to the physical masking of the second reflector from the first. The images in the bottom row are produced by using the combination of LCT and ROP. We observe in this case a significant improvement of the image for the remote target mainly because this method allows us to image one reflector at a time.

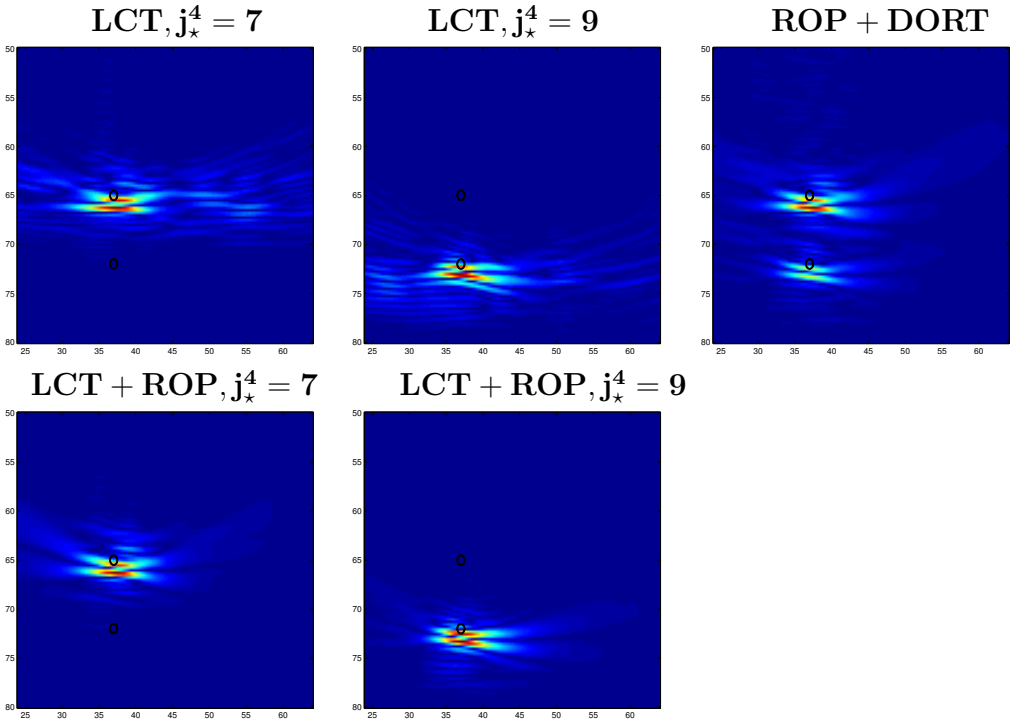

Figure 4.15: Combined medium (Total Field). **Top:** LCT image at $j_\star^4 = 7, 9$, respectively, and bandwidth $B = [0, 4.8]$MHz, the ROP filter combined with DORT at the selected windows and bandwidths shown on Table 4.3. **Bottom:** The LCT+ROP images.

Next, we present the results obtained in isotropic and layered media. We consider first the isotropic medium. The selection criterion of eq. (3.11) for the calculated threshold presented in the center column of Table 4.3, suggests the

windows and bandwidths presented in Table 4.3. These are the couples of $(j_\star^l, B_{j_\star^l})$ at level $l = 4$, where the reflectors are detectable. The LCT window detection test is shown in Figure 4.16. The left plot, provides that we have two targets, one located at window 7 and one located at window 8. In the center and right plots, we plot the the top 10 singular values as a function of frequency for the two selected time-windows. What we see is an anomaly of the first two singular values along the whole frequency band, in both plots. That break in the pattern of the singular values enables us to use the frequency range $B = [0, 30]$ MHz, as we did in Figure 4.10.

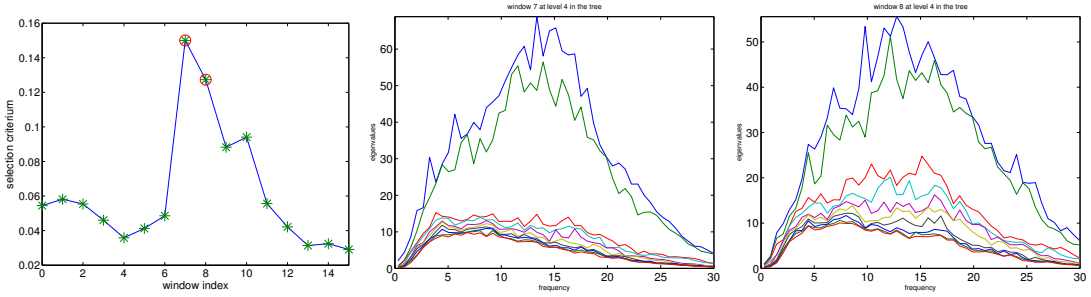

Figure 4.16: Isotropic medium. On the left we see the selection criterion that suggests that we have two targets one located at window 7 and one at window 8. On the center and right plots we see the singular values in the selected windows 7 and 8 respectively.

In the top row of Figure 4.17, the left and the right migration images are obtained using the LCT-based filter. The results are satisfactory only for the scatterer which is closer to the array of transducers. The remote reflector is not clearly detected at the desired window $j_\star^4 = 8$. On the right, we show the image obtained using the ROP filtering method combined with DORT. We observe good results with respect to the first reflector but the amplitude of the image is low in the vicinity of the second reflector. In the bottom row, the migration images obtained using the LCT+ROP filter are illustrated. The second reflector is in this case correctly imaged.

Finally we present the results obtained in the layered medium. The implementation of the detection test taking into account the detection threshold of the right column of Table 4.3, provides the selected time-windows and the corresponding frequency bandwidths depicted in Table 4.3.

We illustrate in Figure 4.18 the LCT detection criterion at level $l = 4$. It suggests that we have two targets: one located at window 6 and one at window 8. On the center and right plots we see the singular values in the selected windows

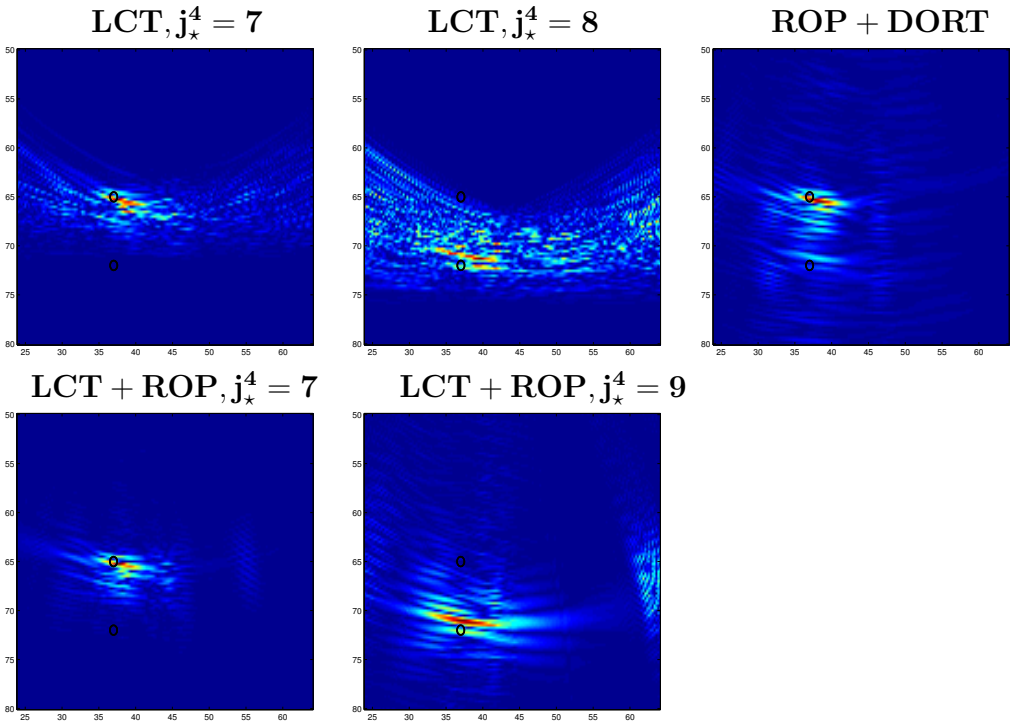

Figure 4.17: Isotropic medium (Total Field). **Top:** LCT image at $j_\star^4 = 7, 8$, respectively, and bandwidth $B = [0, 30]$MHz, the ROP filter combined with DORT at the selected windows and bandwidths shown on Table 4.3. **Bottom:** The LCT+ROP images.

6 and 8, respectively. In both plots, we can see an anomaly of the first singular value (probably the second one) only at the zone of lower frequencies for $B = [0, 3]$ MHz.

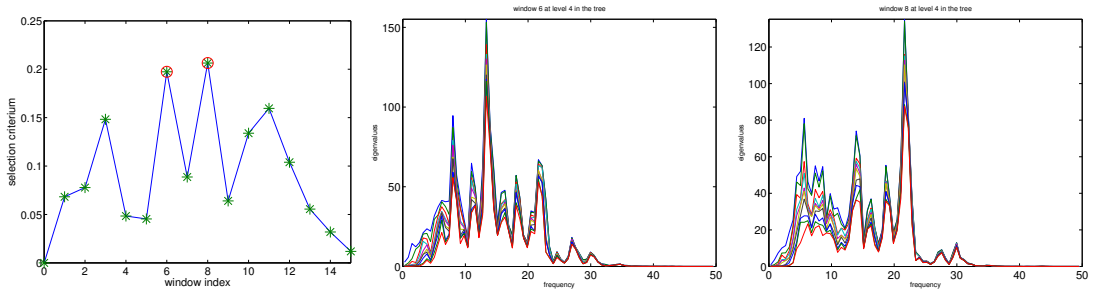

Figure 4.18: Layered medium. On the left we plot the selection criterion that suggests that we have two targets one located at window 6 and one at window 8. On the center and right plots we plot the singular values in the selected windows 6 and 8 respectively.

The resulting KM images obtained from the filtered data in the layered backscattering regime are in Figure 4.19. We can conclude that in this case of clutter as well, the use of LCT+ROP produces the images with the higher SNR.

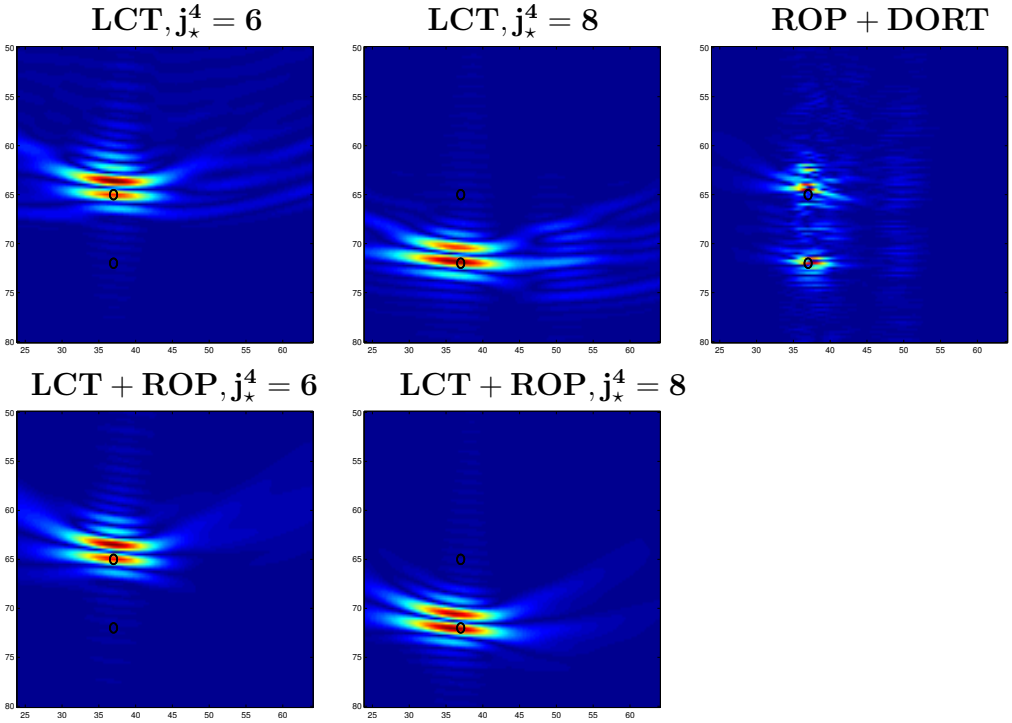

Figure 4.19: Layered medium (Total Field). **Top:** LCT image at $j_\star^4 = 6, 8$, respectively, and bandwidth $B = [0, 3]$MHz, the ROP filter combined with DORT at the selected windows and bandwidths shown on Table 4.3. **Bottom:** The LCT+ROP images.

Conclusion

In this thesis we considered recently developed filtering methodologies for coherent signal enhancement that allow for imaging small defects in strongly scattering media. The data are segmented into time-frequency windows and the windows that contain coherent detectable echoes are selected. The selection is carried out either following the LCT-based methodology as in [14] or a random matrix theory based approach [2]. The LCT-based method selects time-frequency intervals in which the coherent signal is detectable by seeking for a pattern disruption in the behavior of the singular values of the local-cosine transformed response matrix. Random matrix theory is used either with a criterion that relies on the maximal value of the image or in conjunction with a filter that aims at removing multiple scattering contributions from the data. This filter, which we call the rank one projection (ROP), was proposed in [15] and can be also regarded as an autonomous step that can be applied to the time-frequency filtered data provided by the LCT-based algorithm. We show with extensive numerical simulations, carried out in a non-destructive testing setup, that the LCT-based approach benefits by the additional application of ROP and this is the method which provides the images with the higher SNR in all cluttered media configurations considered.

Περίληψη

Θεωρούμε το πρόβλημα της ανίχνευσης και απεικόνισης μικρών ατελειών (defects) σε μέσα με ισχυρή σκέδαση, χρησιμοποιώντας μια ενεργή συστοιχία μετατροπέων που μπορούν να παίξουν τον διττό ρόλο των πομπών και δεκτών. Τα δεδομένα μας είναι ο πίνακας απόκρισης συστοιχίας που συλλέγεται στέλνοντας βραχείς παλμούς από κάθε πηγή και καταγράφοντας την απόκριση του μέσου σε όλους τους δέκτες. Αυτό το πρόβλημα βρίσκει εφαρμογές στη σεισμική απεικόνιση, δηλαδή την απεικόνιση γεωλογικών σχηματισμών του υπεδάφους, καθώς και στον μη καταστροφικό έλεγχο υλικών με τη χρήση υπερήχων. Στην εργασία αυτή επικεντρώσαμε το ενδιαφέρον μας στη δεύτερη εφαρμογή.

Η απεικόνιση σε μέσα με ισχυρή σκέδαση αποτελεί μια σημαντική πρόκληση διότι στα δεδομένα της συστοιχίας κυριαρχεί ο θόρυβος εξαιτίας της πολλαπλής σκέδασης των κυμάτων από τις ανομοιογένειες του μέσου. Για την επιτυχή λύση του προβλήματος της απεικόνισης σε ένα τέτοιο περιβάλλον ακολουθούμε τη μεθοδολογία της συνεπούς βελτίωσης σήματος διαμέσω του φιλτραρίσματος των δεδομένων. Ειδικότερα, θεωρούμε την προσέγγιση της εργασίας [14] και αναζητούμε να επιλέξουμε τα παράθυρα χρόνου-συχνότητας που εμπεριέχουν τις ανακλάσεις από τις ατέλειες που επιθυμούμε να απεικονίσουμε. Η μέθοδος που ακολουθούμε βασίζεται στη χρήση του τοπικού μετασχηματισμού συνημιτόνου (Local Cosine Transform (LCT)). Η επιλογή των παραθύρων χρόνου-συχνότητας συντελείται με την ανίχνευση μιας διαφορετικής συμπεριφοράς των ιδιαζουσών τιμών του μετασχηματισμένου πίνακα απόκρισης ως συνάρτηση της συχνότητας.

Θεωρούμε επίσης δύο διαδικασίες επιλογής παραθύρων που χρησιμοποιούν ιδέες από τη θεωρία τυχαίων πινάκων (random matrix theory). Η πρώτη εξ αυτών, βασίζεται στο αποτέλεσμα της απεικόνισης και πιο συγκεκριμένα στο μέγιστο της εικόνας (κατάλληλα κανονικοποιημένης) που προκύπτει από τα δεδομένα για κάθε παράθυρο χρόνου-συχνότητας.

Η δεύτερη διαδικασία, χρησιμοποιεί ένα φίλτρο (ROP) για να αποβάλλει από τα δεδομένα τις συνεισφορές της πολλαπλούς σκέδασης κι έπειτα επιλέγει τα παράθυρα χρόνου-συχνότητας, για τα οποία η ατέλεια είναι ανιχνεύσιμη, κοιτώντας τη μεγαλύτερη ιδιάζουσα τιμή του φιλτραρισμένου πίνακα απόκρισης. Σε αυτήν την περίπτωση δηλαδή η επιλογή βασίζεται μόνο στα δεδομένα του προβλήματος.

Και στις δύο διαδικασίες είναι απαραίτητη η μελέτη των ιδιοτήτων του πίνακα απόκρισης στο μέσο με ισχυρή σκέδαση απουσία των ατελειών. Καθώς μας ενδιαφέρουν μόνο στατιστικές ιδιότητες του πίνακα απόκρισης δεν είναι απαραίτητο να γίνουν μετρήσεις στο ίδιο μέσο απουσία του σκεδαστή (κάτι που μπορεί να μην είναι πάντα πρακτικά δυνατό). Αρκεί να έχουμε μετρήσεις του πίνακα απόκρισης σε ένα υγιές μέσο (χωρίς ατέλειες) με τα ίδια χαρακτηριστικά πολλαπλής σκέδασης με το μέσο που μας ενδιαφέρει να ελέγξουμε.

Πρέπει να τονίσουμε ότι το φίλτρο ROP που αφορά την επιλογή του πεδίου που έχει υποστεί μόνο απλή σκέδαση (single scattering) είναι πολύ απλό στην εφαρμογή του και μπορεί να συνδυαστεί με το φίλτρο LCT. Η εφαρμογή του επιφέρει σημαντική βελτίωση του λόγου σήματος προς θόρυβο στα αποτελέσματα της απεικόνισης. Αυτό αναδεικνύεται ιδιαιτέρα χρήσιμο όταν το μέσο έχει πολλαπλές ατέλειες.

Μελετήσαμε την απόδοση των διαφορετικών προσεγγίσεων με εκτεταμένες προσομοιώσεις που διεξάγονται στο πλαίσιο δοκιμών μη καταστροφικού ελέγχου υλικών. Οι προσομοιώσεις μας δείχνουν ότι ο συνδυασμός του LCT φίλτρου με το φίλτρο ROP παρέχει τα καλύτερα απεικονιστικά αποτελέσματα.

Acknowledgements

This work was partially supported by the European Research Council Starting Grant, *GA*239959 and the PEFYKA project within the KRIPIS action of the GSRT.

Bibliography

[1] R. Alonso, L. Borcea, G. Papanicolaou, and C. Tsogka. Detection and imaging in strongly backscattering randomly layered media. *Inverse Problems*, 27:025004, 2011.

[2] A. Aubry and A. Derode. Detection and imaging in a random medium: A matrix method to overcome multiple scattering and aberration. *J.APPL.PHYS.*, 106:044903, 2009.

[3] A. Aubry and A. Derode. Random matrix theory applied to acoustic backscattering and imaging in complex media. *Phys. Rev. Lett.*, 102(8):084301, Feb 2009.

[4] A. Aubry and A. Derode. Singular value distribution of the propagation matrix in random scattering media. *Waves in Random and Complex Media*, 20:333–363, 2010.

[5] lorenzo audibert. *Qualitative methods for heterogeneous media.* Theses, Ecole Doctorale Polytechnique, September 2015.

[6] E. Bécache, P. Joly, and C. Tsogka. Etude d'un nouvel élément fini mixte permettant la condensation de masse. *C. R. Acad. Sci. Paris Sér. I Math.*, 324:1281–1286, 1997.

[7] E. Bécache, P. Joly, and C. Tsogka. An analysis of new mixed finite elements for the approximation of wave propagation problems. *SIAM J. Numer. Anal.*, 37:1053–1084, 2000.

[8] E. Bécache, P. Joly, and C. Tsogka. Fictitious domains, mixed finite elements and perfectly matched layers for 2-d elastic wave propagation. *J. of Comput. Acoustics*, 9:1175–1202, 2001.

[9] J. Bérenger. A perfectly matched layer for the absorption of electromagnetic waves. *Journal of Comp. Physics*, 114:185–200, 1994.

[10] Biondo Biondi. *3D Seismic Imaging*. Number 14 in Investigations in Geophysics. Society of Exploration Geophysicists, Tulsa, 2006.

[11] N. Bleistein, J.K. Cohen, and J.W. Stockwell Jr. *Mathematics of multidimensional seismic imaging, migration, and inversion*. Springer, New York, 2001.

[12] L. Borcea, G. Papanicolaou, and C. Tsogka. Interferometric array imaging in clutter. *Inverse Problems*, 21(4):1419–1460, 2005.

[13] L. Borcea, G. Papanicolaou, and C. Tsogka. Adaptive interferometric imaging in clutter and optimal illumination. *Inverse Problems*, 22(4):1405–1436, 2006.

[14] L. Borcea, G. Papanicolaou, and C. Tsogka. Adaptive time-frequency detection and filtering for imaging in heavy clutter. *SIAM Imaging Sciences*, 4(3):827–849, 2011.

[15] L. Borcea, G. Papanicolaou, and C. Tsogka. Time and direction of arrival detection and filtering for imaging in strongly scattering media. *ArXiV:1603.05223*, 2016.

[16] B. Borden. Mathematical problems in radar inverse scattering. *Inverse Problems*, 19:R1–R28, 2002.

[17] Wlodzimierz Bryc, Amir Dembo, and Tiefeng Jiang. Spectral measure of large random hankel, markov and toeplitz matrices. *The Annals of Probability*, 34:1–38, 2006.

[18] R. R. Coifman and Y. Meyer. Remarques sur l'analyse de Fourier a fenêtre. *C.R. Acad. Sci.*, pages 259–261, 1991.

[19] J. C. Curlander and R. N. McDonough. *Synthetic Aperture Radar*. Wiley, New York, 1991.

[20] S. Feng and D. Sornette. Acoustical nondestructive evaluation of heterogeneous materials in the multiple scattering regime. *J. Acoust. Soc. Am.*, 90:1742–1748, 1991.

[21] J. Garnier and G. Papanicolaou. Passive sensor imaging using cross correlations of noisy signals in a scattering medium. *SIAM Imaging Sciences*, 2(2):396–437, 2009.

[22] J. Garnier and K. Solna. Coherent interferometric imaging for synthetic aperture radar in the presence of noise. *Inverse Problems*, 24(5):055001 (pp. 23), 2008.

[23] J. Goodman. *Statistical Optics*. John Wiley & Sons, New York, 1985.

[24] J.P. Groby and C. Tsogka. A time domain method for modeling viscoacoustic wave propagation. *J. of Comput. Acoustics*, 14:201–236, 2006.

[25] J. Garnier H. Ammari and K. *Sølna*. A statistical approach to target detection and localization in the presence of noise. *Waves in Random and Complex Media*, 22:40–65, 2012.

[26] W. R. Hedrick and C. L. Peterson. Image artifacts in real-time ultrasound. *Journal of Diagnostic Medical Sonography*, 11:300–308, 1995.

[27] B. Karamata, M. Laubscher, S. Bourquin, T. Lasser, and P. Lambelet. Multiple scattering in optical coherence tomography. i. investigation and modeling. *J. Opt. Soc. Am. A*, 22:1369–1379, 2005.

[28] B. Karamata, M. Laubscher, S. Bourquin, T. Lasser, and P. Lambelet. Multiple scattering in optical coherence tomography. ii. experimental and theoretical investigation of cross talk in wide-field optical coherence tomography. *J. Opt. Soc. Am. A*, 22:1380–1388, 2005.

[29] V. Kozlov, A. Samokrutov, and V. Shevaldykin. Thickness measurements and flaw detection in concrete using ultrasonic echo method. *Nondestr. Test. Eval.*, 13:73–84, 1997.

[30] S. Mallat. *A wavelet tour of signal processing*. Academic Press, second edition, 1999.

[31] F. Martini, C. J. Bean, S. Dolan, and D. Marsan. Seismic image quality beneath strongly scattering structures and implications for lower crustal imaging : numerical simulations. *Geophys. J. Int.*, 145:423–435, 2001.

[32] Adam Massey, Steven J. Miller, and John Sinsheimer. Distribution of eigenvalues of real symmetric palindromic toeplitz matrices and circulant matrices. *Journal of Theoretical Probability*, 20:637–662, 2007.

[33] T. Nelson, D. Pretorius, A. Hull, M. Riccabona, M. Sklansky, and G. James. Sources and impact of artefacts on clinical three-dimensional ultrasound imaging. *Ultrasound Obset Gynecol.*, 16:374–383, 2000.

[34] C. Prada and M. Fink. Eigenmodes of the time reversal operator: A solution to selective focusing in multiple-target media. *Wave Motion*, 20:151–163, 1994.

[35] C. Prada, S. Manneville, D. Poliansky, and M. Fink. Decomposition of the time reversal operator: Application to detection and selective focusing on two scatterers. *J. Acoust. Soc. Am.*, 99:2067–2076, 1996.

[36] M. C. W. Van Rossum and Th. M. Nieuwenhuizen. Multiple scattering of classical waves: microscopy, mesoscopy, and diffusion. *Reviews of Modern Physics*, 71:313–371, 1999.

[37] C. Tsogka and M. Apostolopoulos. A comparative study of data filtering methods for imaging in strongly scattering media. *Wave Motion*, pages 97–113, 2017.

[38] R. Wagner, S. Smith, J. Sandrik, and H. Lopez. Statistics of speckle in ultrasound b-scans. *IEEE Trans. Son. Ultrason.*, 30:156–163, 1983.

[39] Y. Ziadé, H. Roussel, M. Lesturgie, and W. Tabbara. A coherent model of forest propagation: application to detection and localization of targets using the dort method. *IEEE Trans. Antennas Propag.*, 56:1048–1057, 2008.